

Lattice Boltzmann simulation reveals supercritical bifurcation in flow mode transitions of power-law fluids in the four-roll mill

Yuan Yu (余愿)^{1, 2, 3} Xiao Jiang (江校)^{1, a)} Qingqing Gu (顾青青)^{4, b)} Chuandong Lin (林传栋)⁵ Qingyong Zhu (朱庆勇)^{6, c)} and Hai-zhuan Yuan (袁海专)^{1, d)}

¹⁾*School of Mathematics and Computational Science, Xiangtan University, Xiangtan 411105, China*

²⁾*National Center for Applied Mathematics in Hunan, Xiangtan 411105, China*

³⁾*Hunan Key Laboratory for Computation and Simulation in Science and Engineering, Xiangtan University, Xiangtan 411105, China*

⁴⁾*School of Energy and Power Engineering, University of Shanghai for Science and Technology, Shanghai 200093, China*

⁵⁾*Sino-French Institute of Nuclear Engineering and Technology, Sun Yat-sen University, Zhuhai 519082, China*

⁶⁾*School of Aeronautics and Astronautics, Sun Yat-sen University, Shenzhen 518107, China*

(Dated: 9 January 2025)

The four-roll mill has been traditionally viewed as a device generating simple extensional flow with a central stagnation point. Our systematic investigation using a two-relaxation-time regularized lattice Boltzmann (TRT-RLB) model reveals unexpected richness in the flow physics, identifying two previously unreported supercritical bifurcation modes: a quadrifoliate vortex mode featuring four symmetrical counter-rotating vortices, and a dumbbell-shaped quad-vortex mode where vortices detach from but remain symmetric about the stagnation point. The numerical framework, representing the first successful extension of TRT-RLB method to power-law fluid dynamics, enables comprehensive mapping of flow characteristics across Reynolds numbers ($1 \leq Re \leq 50$), power-law indices ($0.7 \leq n \leq 1.3$), and geometric configurations. The transition from quadrifoliate vortex mode exhibits distinct pathways depending on the power-law index: at relatively small n , the flow undergoes a direct supercritical bifurcation to simple extensional flow, while at relatively large n , it evolves through an intermediate dumbbell-shaped state. Among geometric parameters, the roller radius r emerges as the dominant factor controlling bifurcation points and vortex dimensions, whereas the roller-container gap δ exerts minimal influence on flow regimes. The transitions between flow modes can be precisely characterized through the evolution of vortex dimensions and velocity gradients at the stagnation point, providing quantitative criteria for flow regime identification. These findings enrich our fundamental understanding of bifurcation phenomena in extensional devices and provide quantitative guidelines for achieving desired flow patterns in four-roll mill applications.

I. INTRODUCTION

While extensive research has explored four-roll mill dynamics using various numerical approaches, the simulation of power-law fluids in such complex geometries presents unique challenges. Traditional numerical methods often struggle with the nonlinear constitutive relationships and complex boundary conditions. The two-relaxation-time regularized lattice Boltzmann (TRT-RLB) method offers distinct advantages for such systems, including superior numerical stability and efficient handling of curved boundaries. This work represents the first successful extension of the TRT-RLB methodology to power-law fluid dynamics in four-roll mill configurations, enabling comprehensive investigation of flow mode transitions and bifurcation phenomena.

To achieve steady-state deformation of droplets or cells at a prescribed strain rate, a continuous extensional flow (also known as hyperbolic flow) must be generated in the fluid. This

flow configuration is characterized by a stagnation point, where the local velocity vanishes while maintaining a non-zero strain rate. The four-roll mill, as shown in Fig. 1, was invented by Taylor (1934) to generate simple extensional flow with a stagnation point. The device comprises four cylindrical rollers with their axes arranged in a square configuration, positioned symmetrically and parallel to one another. The simple extensional flows with stagnation points, generated by four-roll mills or similar devices, have been instrumental in various research areas: investigating drop and cell deformation and breakup (Kumar *et al.*, 2019; Bryngelson and Freund, 2019; Narayan *et al.*, 2020; Hymel, Lan, and Khismatullin, 2020; Tu *et al.*, 2023; Xie and Leonetti, 2023), conducting extensional rheometry of complex fluids (Haward *et al.*, 2012a,b), and examining macromolecular dynamics (Schroeder *et al.*, 2003a; Hsiao *et al.*, 2016; Zhou and Schroeder, 2016; Sasmal *et al.*, 2017) and elastic instabilities (Arratia *et al.*, 2006; Poole, Alves, and Oliveira, 2007; Haward, McKinley, and Shen, 2016).

Research on non-Newtonian fluids using the four-roll mill has focused on several key areas. In polymer studies, Milliken and Leal (1991) employed a computer-controlled four-roll mill to investigate polymer drop deformation and breakup in immiscible Newtonian fluids. The dynamics of polymer systems was further explored by Lee and Muller (1999), who examined isolated polymer chains in dilute solutions under steady simple

^{a)}Electronic mail: xjiang@smail.xtu.edu.cn

^{b)}Author to whom correspondence should be addressed: guqq@usst.edu.cn

^{c)}Electronic mail: mcszqy@mail.sysu.edu.cn

^{d)}Electronic mail: yhz@xtu.edu.cn

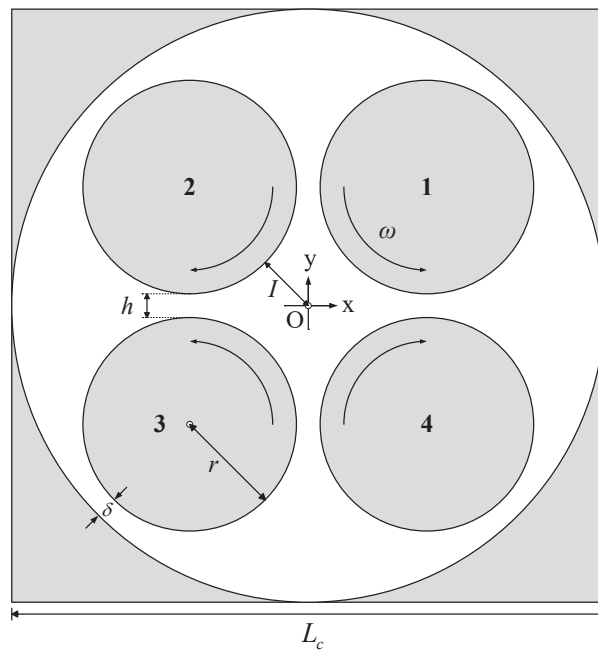


FIG. 1: Cross-sectional schematic of the four-roll mill configuration. The rollers of length L_z rotate at angular velocity ω . The geometric parameters include: roller radius r , gap between adjacent rollers h , gap between rollers and container wall δ , and container diameter L_c . Each roller rotates with equal speed but with alternating directions as indicated by the arrows. The flow is assumed two-dimensional due to the sufficiently long rollers ($L_z \gg L_c$).

extensional flow using flow light scattering, and by Schroeder *et al.* (2003b), who observed highly extended *E. coli* DNA molecules through fluorescence microscopy. Investigations into viscoelastic effects include studies by Trettheway and Leal (2001) and Ha and Leal (2001) on the deformation and relaxation of Newtonian droplets in Boger fluids, while D'Avino and Maffettone (2017) numerically analyzed the dispersive mixing of particles in viscoelastic fluids. The optical properties of non-Newtonian fluids have also been extensively studied, with several researchers investigating flow birefringence phenomena of polymers in simple extensional flow (Crowley *et al.*, 1976; Fuller and Leal, 1980, 1981; Dunlap and Leal, 1987). These diverse investigations of polymer dynamics, viscoelastic effects, and flow birefringence highlight the four-roll mill as an indispensable apparatus for probing the fundamental physics of non-Newtonian fluids.

Various control techniques of the four-roll mill have been developed to achieve stable simple extensional flow and keep particles or droplets at the stagnation point. Initially, Taylor's manually controlled four-roll mill (Taylor, 1934) often resulted in unstable simple extensional flow. Bentley and Leal (1986) designed a computer-controlled four-roll mill, which stabilized the flow field and maintained particles at its center through automated roller speed adjustment. Subsequent studies focused on different control strategies: Balasuriya and Padberg-Gehle (2013) proposed a method based on velocity perturbation control to maintain particles on hyperbolic trajectories, while Vona and Lauga (2021) developed machine learning algorithms for droplet stabilization. While these control techniques have achieved considerable success, their emphasis on technolog-

ical solutions rather than fundamental flow physics suggests an incomplete understanding of the underlying flow mechanisms. A comprehensive investigation of flow modes and their transitions in the four-roll mill is therefore essential for both scientific understanding and practical applications.

Beyond control techniques, extensive research has explored how the geometric parameters of four-roll mills influence the generated simple extensional flow. Bentley (1985) emphasized the importance of moderate mill dimensions: sufficiently large to accommodate highly deformed droplets before breakup, yet small enough to maintain stable simple extensional flow while minimizing construction and filling costs. Through experimental studies, Lagnado and Leal (1990) observed that while homogeneous simple extensional flow develops in the central region at specific Reynolds numbers Re , stable vortices emerge along the top and bottom walls when Re exceeds a critical value. This transition was primarily attributed to the ratio of roller length to the gap between adjacent rollers. In a numerical investigation comparing various mill configurations, Higdon (1993) determined that optimal simple extensional flow occurs when the roller radius r , the gap h between adjacent rollers, and the square container size L satisfy $r/(h/2 + r) = 0.625$ and $L/(h/2 + r) > 3.0$. Andreotti, Douady, and Couder (2001) proposed that simple extensional flow requires the gap h , roller radius r , and distance I from rollers to the mill center to satisfy:

$$(r+I)^2 = 2(r+h/2)^2, \quad (1)$$

where $(r+I)$ represents the distance from roller center to mill center, and $(r+h/2)$ denotes the distance from roller center to axis. They further outlined specific geometric conditions to

minimize the impact of roller-container spacing on central simple extensional flow. A circular container was recommended over a square one, as corner regions in square containers generate complex recirculating flows that may influence central flow modes. Furthermore, excessive gaps δ between rollers and container walls can induce Couette-Taylor-like flows around rollers, characterized by superposed toroidal sectors with alternating rotation directions. Similarly, insufficient gaps between adjacent rollers may produce complex recirculating flows in the central region. Akbaridoust, Philip, and Marusic (2018) experimentally demonstrated that reducing inter-roller gaps and increasing roller radius enhances the strain rate at the stagnation point, attributed to increased linear roller velocity and consequent flow velocity gradients. Notably, both Andreotti, Douady, and Couder (2001) and Akbaridoust, Philip, and Marusic (2018) found that the stagnation point strain rate is directly proportional to roller angular speed, and that lower fluid viscosity leads to more unstable simple extensional flow.

Previous research on four-roll mills has primarily focused on optimizing control techniques and geometric configurations to achieve stable simple extensional flow in the central region, thereby maintaining particles or droplets at the stagnation point. However, a systematic investigation of the underlying flow mechanisms remains unexplored. While extensive research has explored four-roll mill dynamics using various numerical approaches (Wang, Han, and Yu, 2012), the simulation of power-law fluids in such complex geometries presents unique challenges. Traditional numerical methods often struggle with the nonlinear constitutive relationships and complex boundary conditions. The two-relaxation-time regularized lattice Boltzmann (TRT-RLB) method offers distinct advantages for such systems, including superior numerical stability and efficient handling of curved boundaries (Yu *et al.*, 2023, 2025). This study examines the flow mechanisms of Newtonian and power-law fluids in the four-roll mill, revealing previously unreported flow modes. A distinctive mode is observed where the flow deviates from simple extensional behavior, forming four symmetrical vortices around the central point with alternating rotational directions between adjacent vortices. While the central point remains stagnational, it maintains simple extensional flow in its immediate vicinity. The correlation between central point shear rate, vortex formation, and governing parameters such as Reynolds number Re , power-law index n , roller-container gap δ , and roller radius r is investigated, with special attention to the critical conditions for vortex suppression. For systematic numerical investigation of various flow modes, the TRT-RLB model (Yu *et al.*, 2023) is employed, ensuring high accuracy and stability in power-law fluid simulations. High-order accuracy near boundary regions is achieved through the implementation of the one-point second-order curved boundary scheme (Tao *et al.*, 2018). The remainder of this paper is structured as follows: Section I reviews the research progress on four-roll mills; Section II presents the problem description and governing equations; Section III details the TRT-RLB model, boundary condition implementation, and numerical validation; Section IV discusses the simulation results; and Section V summarizes the main findings.

II. PROBLEM DESCRIPTION AND GOVERNING EQUATION

A. Structure of the four-roll mill

Fig. 1 shows the cross-sectional view of the four-roll mill used in this study, where the rollers are assumed to be sufficiently long such that the flow can be approximated as two-dimensional (2D) in the central region. This idealization is justified when the roller length is much larger than other geometric dimensions, allowing us to focus on the essential flow physics in the transverse plane. The origin of the coordinate system, denoted as point $O(0,0)$, coincides with the center of the mill. The circular container has a diameter of L_c , and the gap between adjacent rollers is h . Four identical rollers of radius r are symmetrically arranged around point O , labeled as rollers 1 through 4, with their centers located at $(r+h/2, r+h/2)$, $(-r-h/2, r+h/2)$, $(-r-h/2, -r-h/2)$, and $(r+h/2, -r-h/2)$, respectively. The distance from each roller edge to point O is denoted as l , yielding a center-to-origin distance of $(l+r)$, which satisfies the geometric relationship proposed by Andreotti, Douady, and Couder (2001) in Eq. (1).

Given the assumption of infinite roller length L_z along the z -axis, the flow field exhibits no variation in the longitudinal direction ($\partial u/\partial z = 0$) and no axial velocity component ($u_z = 0$). Each roller rotates at a constant angular velocity ω , producing a uniform tangential velocity of $U_c = \omega r$ at the roller surface. To establish simple extensional flow near point O , adjacent rollers rotate with equal angular speeds but in opposite directions: rollers 2 and 4 rotate clockwise, while rollers 1 and 3 rotate counterclockwise.

B. Governing equations

The 2D continuity equation and momentum equations for the generalized Newtonian fluid used in this study are as follows:

$$\frac{\partial \rho}{\partial t} + \frac{\partial(\rho u_\alpha)}{\partial x_\alpha} = 0, \quad (2a)$$

$$\frac{\partial(\rho u_\alpha)}{\partial t} + \frac{\partial(\rho u_\alpha u_\beta)}{\partial x_\beta} = -\frac{\partial(p\delta_{\alpha\beta})}{\partial x_\alpha} + \frac{\partial\tau_{\alpha\beta}}{\partial x_\beta}. \quad (2b)$$

where ρ denotes fluid density, u_α represents velocity component in the α direction, x_α is the spatial coordinate, t represents time, p is pressure, $\delta_{\alpha\beta}$ is the Kronecker delta, and $\tau_{\alpha\beta}$ represents the stress tensor, given by

$$\tau_{\alpha\beta} = \mu \dot{\gamma}_{\alpha\beta}, \quad (3)$$

where $\dot{\gamma}_{\alpha\beta}$ is shear-rate tensor and μ is dynamic viscosity. For power-law fluids, the effective viscosity is

$$\mu = \mu_0 |\dot{\gamma}|^{n-1}, \quad (4)$$

where μ_0 and n represent viscosity coefficient and power-law index, respectively. The shear rate $|\dot{\gamma}|$ is defined as $|\dot{\gamma}| = \sqrt{2D_{II}}$,

with D_{Π} being the second invariant of the strain rate tensor $S_{\alpha\beta}$ and expressed as

$$D_{\Pi} = \sum_{\alpha,\beta=1}^2 S_{\alpha\beta} S_{\alpha\beta}, \quad (5)$$

where $S_{\alpha\beta}$ is defined as

$$S_{\alpha\beta} = \frac{1}{2} (\partial_{\beta} u_{\alpha} + \partial_{\alpha} u_{\beta}), \quad (6)$$

leading to the explicit expression for $|\dot{\gamma}|$:

$$|\dot{\gamma}| = \sqrt{2(\partial_x u_x)^2 + 2(\partial_y u_y)^2 + (\partial_y u_x + \partial_x u_y)^2}. \quad (7)$$

For power-law fluids, the effective Reynolds number Re is defined using the characteristic length h and velocity U_c :

$$Re = \frac{\rho U_c^{2-n} h^n}{\mu_0}. \quad (8)$$

III. NUMERICAL METHODS AND VALIDATION

In the following sections, the TRT-RLB model is introduced in III A, the one-point second-order curved boundary scheme is described in III B, the model is validated using power-law fluids in channel flow and Taylor-Couette flow problems in III C, and the grid independence analysis is conducted in III D.

A. Two-relaxation-time regularized lattice Boltzmann model

The TRT-RLB model proposed by Yu *et al.* (2023) is employed in this study to ensure superior numerical stability and accuracy compared to other collision models. Its evolution equation is expressed as

$$\begin{aligned} f_i(x_{\alpha} + e_{i\alpha}\Delta t, t + \Delta t) &= f_i^{eq}(x_{\alpha}, t) + \left(1 - \frac{1}{\tau_1}\right) w_i \frac{\mathcal{H}_{i,\alpha}}{c_s^2} \mathcal{A}_{\alpha}^{neq} \\ &+ \left(1 - \frac{1}{\tau_1}\right) w_i \frac{\mathcal{H}_{i,\alpha\beta}}{2c_s^4} \mathcal{A}_{\alpha\beta}^{neq} \\ &+ \left(1 - \frac{1}{\tau_2}\right) w_i \frac{\mathcal{H}_{i,\alpha\beta\gamma}}{6c_s^6} \mathcal{A}_{\alpha\beta\gamma}^{neq} \\ &+ \left(1 - \frac{1}{2\tau_1}\right) F_i \Delta t + G_i \Delta t, \end{aligned} \quad (9)$$

where f_i represents the particle distribution function in the i -th direction, and discrete velocity space $DdQq$. The term $e_{i\alpha}$ denotes the discrete velocity in the i -th direction of the $DdQq$. τ_1 and τ_2 are dimensionless relaxation times, while w_i and c_s represent the weight coefficients and lattice sound speed, respectively. The equilibrium distribution function f_i^{eq} is represented by a third-order Hermite expansion, given by

$$f_i^{eq} = w_i \rho \left\{ \mathcal{H}_i + \frac{\mathcal{H}_{i,\alpha}}{c_s^2} u_{\alpha} + \frac{\mathcal{H}_{i,\alpha\beta}}{2c_s^4} u_{\alpha} u_{\beta} + \frac{\mathcal{H}_{i,\alpha\beta\gamma}}{6c_s^6} u_{\alpha} u_{\beta} u_{\gamma} \right\}, \quad (10)$$

where ρ is the density, satisfying the equation $p = \rho c_s^2$. The Hermite polynomials are defined as follows:

$$\mathcal{H}_i = 1,$$

$$\mathcal{H}_{i,\alpha} = e_{i\alpha},$$

$$\mathcal{H}_{i,\alpha\beta} = e_{i\alpha} e_{i\beta} - c_s^2 \delta_{\alpha\beta},$$

$$\mathcal{H}_{i,\alpha\beta\gamma} = e_{i\alpha} e_{i\beta} e_{i\gamma} - c_s^2 (e_{i\alpha} \delta_{\beta\gamma} + e_{i\beta} \delta_{\gamma\alpha} + e_{i\gamma} \delta_{\alpha\beta}),$$

and their non-equilibrium moments are

$$\mathcal{A}_{\alpha}^{neq} = \sum_i \mathcal{H}_{i,\alpha} (f_i - f_i^{eq}), \quad (11a)$$

$$\mathcal{A}_{\alpha\beta}^{neq} = \sum_i \mathcal{H}_{i,\alpha\beta} (f_i - f_i^{eq}), \quad (11b)$$

$$\mathcal{A}_{\alpha\beta\gamma}^{neq} = \sum_i \mathcal{H}_{i,\alpha\beta\gamma} (f_i - f_i^{eq}). \quad (11c)$$

G_i in Eq. (9) is the compensatory source term added to eliminate error terms when recovering the NS equations. The expression for G_i is given by

$$G_i = -w_i \frac{\mathcal{H}_{i,\alpha\beta}}{6c_s^6} \left(1 - \frac{1}{2\tau_1}\right) \partial_{\gamma} \Phi_{\alpha\beta\gamma}, \quad (12)$$

where

$$\Phi_{\alpha\beta\gamma} = \begin{cases} \rho u_x^3, & \alpha = \beta = \gamma = x, \\ \rho u_y^3, & \alpha = \beta = \gamma = y, \\ 0, & \text{otherwise,} \end{cases} \quad (13)$$

$$\partial_{\gamma} \Phi_{\alpha\beta\gamma} = \partial_x (\rho u_x^3) \delta_{\alpha x} \delta_{\beta x} + \partial_y (\rho u_y^3) \delta_{\alpha y} \delta_{\beta y}. \quad (14)$$

Forcing term F_i in Eq. (9) is

$$F_i = w_i \left\{ \frac{\mathcal{H}_{i,\alpha}}{c_s^2} F_{\alpha} + \frac{\mathcal{H}_{i,\alpha\beta}}{2c_s^4} (F_{\alpha} u_{\beta} + u_{\alpha} F_{\beta}) \right\}. \quad (15)$$

The D2Q9 discrete velocity model is used in this paper. Its velocity sets are given by

$$\begin{pmatrix} e_{ix} \\ e_{iy} \end{pmatrix} = c \begin{bmatrix} 0 & 1 & 0 & -1 & 0 & 1 & -1 & -1 & 1 \\ 0 & 0 & 1 & 0 & -1 & 1 & 1 & -1 & -1 \end{bmatrix}, \quad (16)$$

and the corresponding weights are $w_0 = 4/9$, $w_{1,\dots,4} = 1/9$, $w_{5,\dots,8} = 1/36$. The speed of sound is $c_s = c/\sqrt{3}$, where $c = \Delta x/\Delta t$ is lattice speed. Δx and Δt are the lattice spacing and time step, respectively. The local density ρ and velocity u_{α} are calculated from the distribution function f_i :

$$\sum_i f_i = \sum_i f_i^{eq} = \rho, \quad (17)$$

$$\sum_i e_{i\alpha} f_i + \frac{\Delta t}{2} F_{\alpha} = \rho u_{\alpha}. \quad (18)$$

The viscosity of fluid is related to τ_1 :

$$\mu = \rho c_s^2 (\tau_1 - 0.5) \Delta t. \quad (19)$$

Following Yu *et al.* (2023), the relaxation time τ_2 is set to 1.6 to ensure robust numerical stability when simulating power-law fluids with wide-ranging viscosity variations.

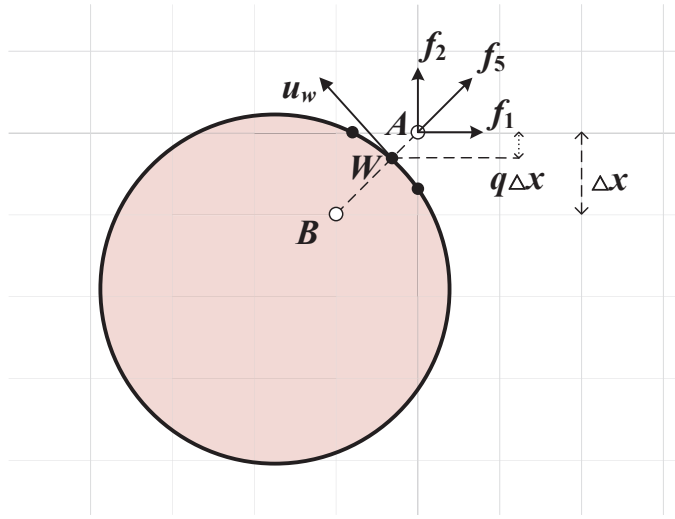


FIG. 2: Schematic of the one-point second-order curved boundary scheme, where $x_{\alpha,A}$, $x_{\alpha,W}$, and $x_{\alpha,B}$ denote the fluid node, boundary point, and solid node, respectively.

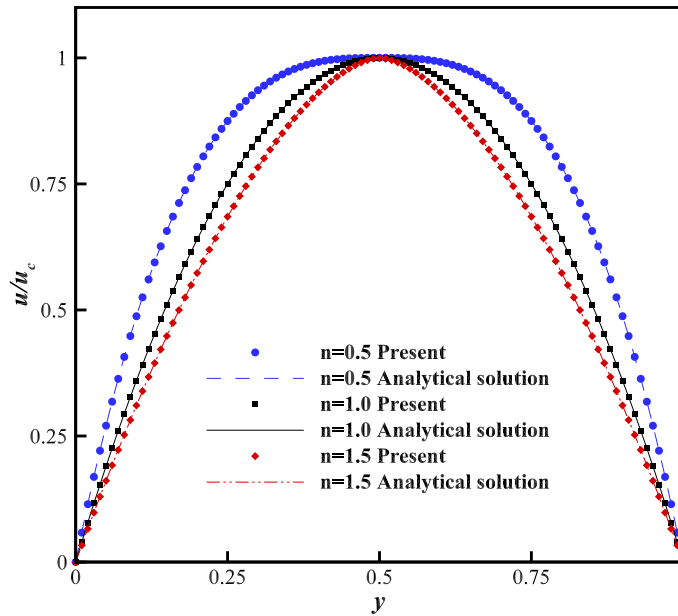


FIG. 3: Comparison between numerical results (symbols) and analytical solutions (lines) for force-driven power-law channel flow at $Re = 10$ with power-law indices $n = 0.5, 1.0,$ and 1.5 .

B. Implementation of boundary condition

The four-roll mill geometry features curved boundaries at both the rollers and container walls. To accurately resolve these curved boundaries, we implement the one-point second-order interpolation scheme developed by Tao *et al.* (2018). This method not only achieves second-order accuracy but also maintains high computational efficiency through its straightforward parallelization. As illustrated in Fig. 2, the scheme considers

three key points along a straight line intersecting the boundary: $x_{\alpha,A}$ denotes the nearest fluid node to the curved boundary, $x_{\alpha,W}$ represents the intersection point on the curved boundary itself, and $x_{\alpha,B}$ indicates the first solid node inside the boundary. The distribution function at point A can be expressed as

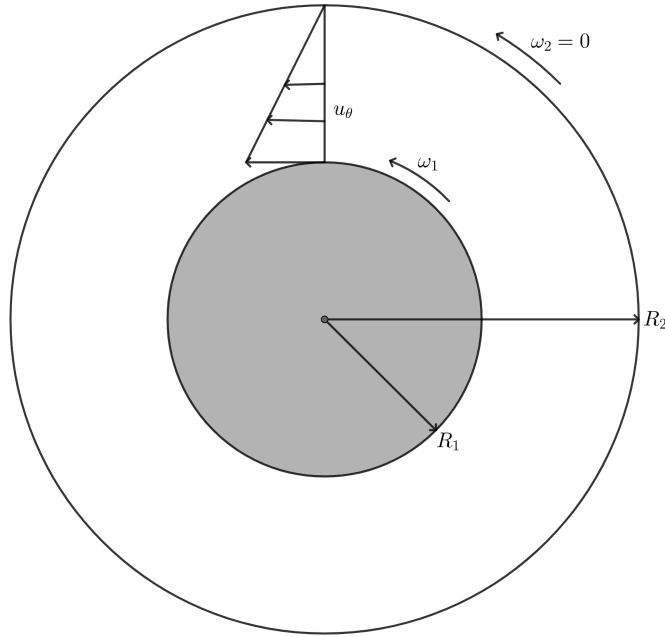


FIG. 4: Schematic of Taylor-Couette flow: an inner cylinder of radius R_1 rotating at angular velocity ω_1 , and a stationary outer cylinder of radius R_2 . This configuration serves as a benchmark case for validating the curved boundary treatment.

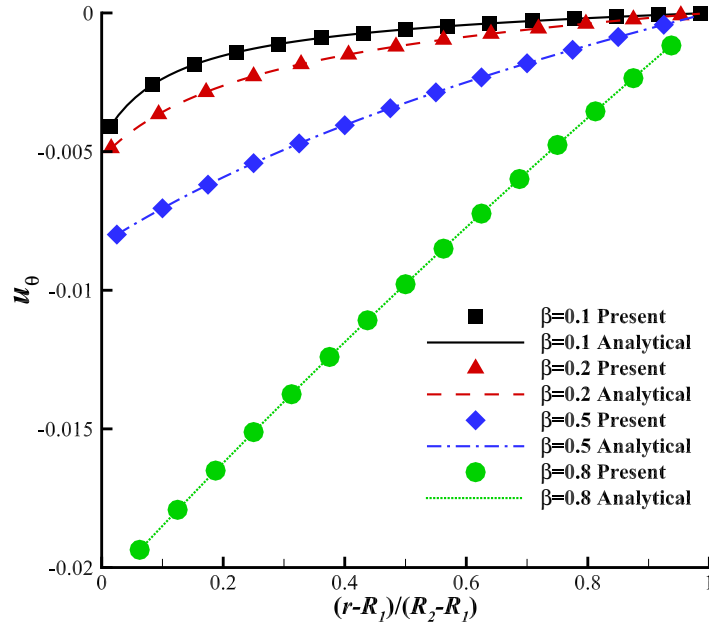


FIG. 5: Velocity profiles of Taylor-Couette flow for different radius ratios ($\beta = 0.1 \sim 0.8$). Symbols represent numerical results and lines denote analytical solutions.

(Tao *et al.*, 2018)

$$f_i(x_{\alpha,A}, t + \Delta t) = \frac{1}{1+q} \left(f_i^{eq}(u_\beta(x_{\alpha,W}, t + \Delta t), \rho(x_{\alpha,A}, t)) + f_i^{neq}(x_{\alpha,A}, t) + q f_i'(x_{\alpha,A}, t) \right), \quad (20)$$

where \bar{i} satisfies $e_{i\alpha} = -e_{i\alpha}$. $f_i^{eq}(u_\beta(x_{\alpha,W}, t + \Delta t), \rho_A(t))$ represents the equilibrium distribution function with the velocity at point W and density at point A . $f_i^{neq}(x_{\alpha,A}, t)$ represents the non-equilibrium distribution function at A . $f_i'(x_{\alpha,A}, t)$ denotes

TABLE I: Grid independence test of the four-roll mill problem for power-law fluid: Dimensionless velocity u_x/u_c and shear rate $|\dot{\gamma}|$ at steady state for different grid sizes N^2 and power-law index n .

$N \times N$	u_x/u_c			$ \dot{\gamma} $		
	$n = 0.7$	$n = 1.0$	$n = 1.3$	$n = 0.7$	$n = 1.0$	$n = 1.3$
500×500	1.5158	1.5352	1.5457	3.530E-03	2.959E-03	7.797E-04
600×600	1.5136	1.5347	1.5463	3.525E-03	2.960E-03	7.806E-04
700×700	1.5131	1.5350	1.5470	3.521E-03	2.961E-03	7.813E-04
800×800	1.5121	1.5349	1.5473	3.518E-03	2.961E-03	7.816E-04
900×900	1.5117	1.5349	1.5477	3.518E-03	2.962E-03	7.820E-04
1000×1000	1.5113	1.5349	1.5479	3.517E-03	2.963E-03	7.821E-04

the post-collision but pre-streaming distribution function at A . The parameter q represents the relative distance from the boundary point A to the point W of solid surface, defined as $q = |x_{\alpha,W} - x_{\alpha,A}| / |x_{\alpha,B} - x_{\alpha,A}|$.

C. Numerical validation

Two benchmark cases are employed to validate our numerical implementation: force-driven channel flow of power-law fluids for validating the power-law model, and Taylor-Couette flow for verifying the accuracy of the one-point second-order curved boundary scheme. Since our focus is on steady-state solutions, the convergence criterion is defined as:

$$E_u = \max\left(\left|\frac{u_\alpha(x_\alpha, t + 10000\Delta t) - u_\alpha(x_\alpha, t)}{U_c}\right|\right) < 10^{-7}, \quad (21)$$

where E_u represents the maximum relative velocity difference over a period of 10000 time steps.

1. Power-law fluid channel flow

For a force-driven channel filled with power-law fluid, the analytical velocity profile is given by (Pontrelli, Ubertini, and Succi, 2009):

$$u(y) = u_c \left[1 - \left(\frac{|y - \frac{H}{2}|}{\frac{H}{2}} \right)^{(n+1)/n} \right], \quad (22)$$

where H denotes the channel height (characteristic length) and u_c represents the maximum velocity (characteristic velocity). The latter is expressed as (Pontrelli, Ubertini, and Succi, 2009):

$$u_c = \left(\frac{F_x}{\mu_0} \right)^{1/n} \left(\frac{n}{n+1} \right) \left(\frac{H}{2} \right)^{(n+1)/n}, \quad (23)$$

where F_x represents the body force in the x -direction.

For the numerical validation, we set the following parameters: channel height $H = 1$, maximum velocity $u_c = 0.01$, and lattice speed $c = 1$. The computational domain is discretized with a grid size of $N_x \times N_y = 10 \times 100$, yielding a spatial resolution of $\Delta x = H/N_x = 0.1$. The Reynolds number is fixed at

$Re = 10$, from which the viscosity coefficient is determined as $\mu_0 = \rho u_c^{2-n} H^n / Re$.

It is worth noting that while traditional TRT implementations achieve no-slip conditions through the magic parameter $\Lambda = 3/16$ (Ginzburg, Verhaeghe, and d'Humières, 2008), this constraint cannot be simultaneously satisfied with our choice of $\tau_2 = 1.6$, which is essential for maintaining numerical accuracy and stability across a wide range of viscosities. Therefore, the moment-based boundary scheme (Reis, 2020) is implemented at the upper and lower walls to ensure no-slip conditions without relying on the magic parameter constraint. The numerical simulations are performed for three different power-law indices ($n = 0.5, 1.0, 1.5$), and the resulting normalized velocity profiles are compared with the analytical solutions. As demonstrated in Fig. 3, the excellent agreement between numerical and analytical results validates the implementation of our power-law model.

2. Taylor-Couette flow

To validate the accuracy of the one-point second-order scheme in handling curved moving boundaries, we employ the Taylor-Couette flow (Tao *et al.*, 2018; Zhao and Yong, 2017) as a benchmark case. As illustrated in Fig. 4, this flow configuration features fluid confined between two concentric cylinders: an inner cylinder of radius R_1 rotating at angular velocity ω_1 , and a stationary outer cylinder of radius R_2 , providing an ideal test case for curved moving boundary treatment. The steady-state analytical solution for the velocity profile is given by (Tao *et al.*, 2018):

$$u_\theta = \frac{(R_1^2 - \beta^2 r^2) \omega_1}{(1 - \beta^2) r}, \quad u_r = 0, \quad (24)$$

where u_θ and u_r are the angular and radial velocity components, respectively, r is the radial distance, and the parameter β represents the ratio of radius R_1 and R_2 . In simulations, the detailed setup are given in Tao *et al.* (2018). The velocity profiles for $\beta = 0.1 \sim 0.8$ are shown in Fig. 5, demonstrating perfect agreement with the analytical solutions. Thus the one-point second-order curved boundary scheme is validated in this study.

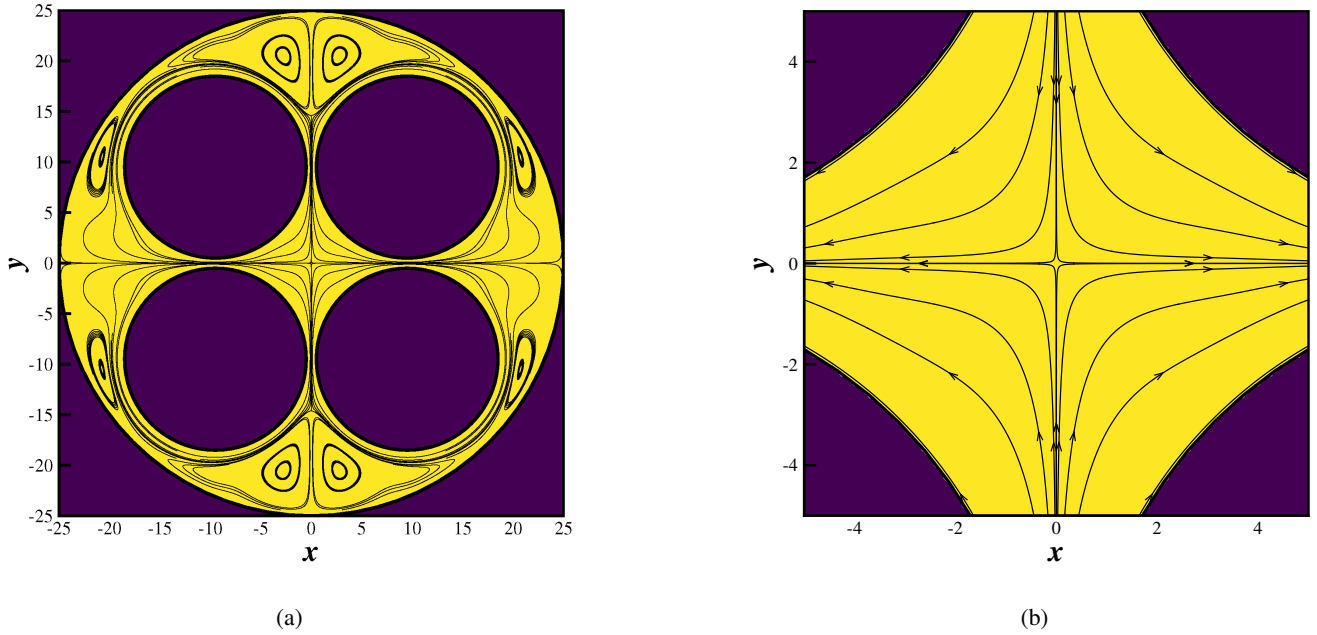


FIG. 6: Streamline patterns in the four-roll mill for Newtonian fluid ($n = 1$) at $Re = 50$ with $h = 1$, $r = 9$, and $\delta \approx 2.56$: (a) entire flow domain and (b) central region. Yellow and purple regions represent fluid and solid domains, respectively.

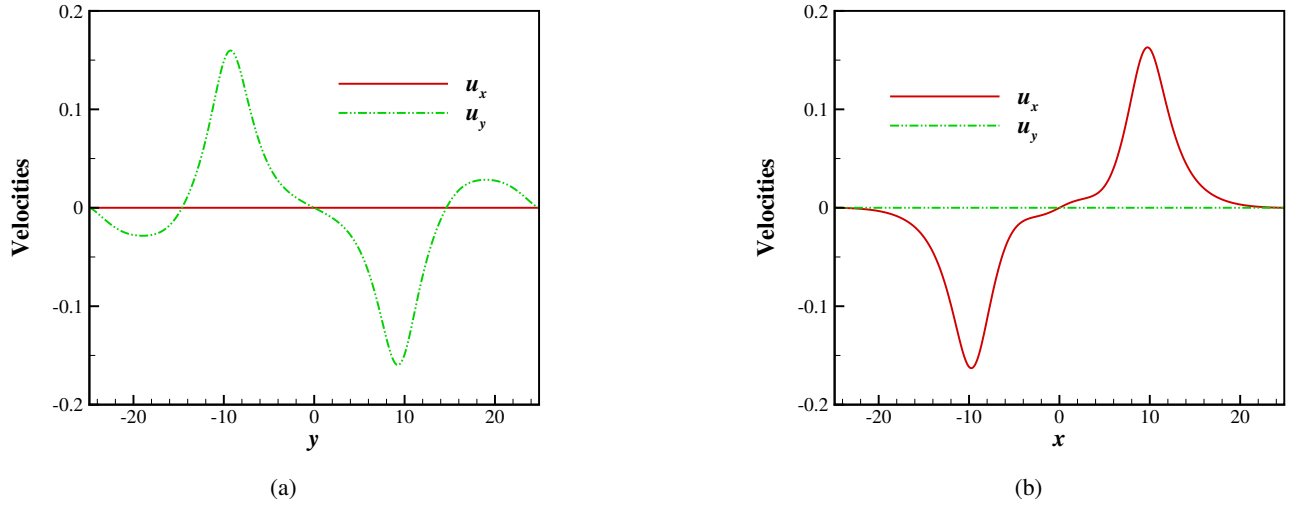


FIG. 7: Velocity distributions characterizing simple extensional flow in the four-roll mill at $Re = 50$ for Newtonian fluid ($n = 1$): (a) u_x and u_y along the y -axis and (b) u_x and u_y along the x -axis. The geometric parameters are $h = 1$, $\delta \approx 2.56$, and $r = 9$. The profiles demonstrate central symmetry about the stagnation point O and the absence of cross-axial fluid transport ($u_x = 0$ along y -axis and $u_y = 0$ along x -axis).

D. Grid convergence study

A grid convergence analysis was performed to ensure the spatial resolution independence of the numerical results for most flow conditions. Six different grid resolutions were examined: $N^2 = 500^2$, 600^2 , 700^2 , 800^2 , 900^2 , and 1000^2 . The geometric configuration of the four-roll mill was specified with $r = 9.5$, $L_c = 50$, and $h = 1$, yielding $I \approx 4.64$ and

$\delta \approx 1.36$. The flow conditions were characterized by $Re = 10$ and $\mu_0 = 0.002$. Two quantities were monitored as convergence metrics: the x -direction velocity u_x at the midpoint between rollers 1 and 4, and the shear rate magnitude $|\dot{\gamma}|$ at the central point O (see Fig. 1). The results are presented in Table I. As the variations in both metrics become negligible for grid resolutions of 800^2 and above, this resolution was adopted for subsequent simulations unless otherwise specified. It should

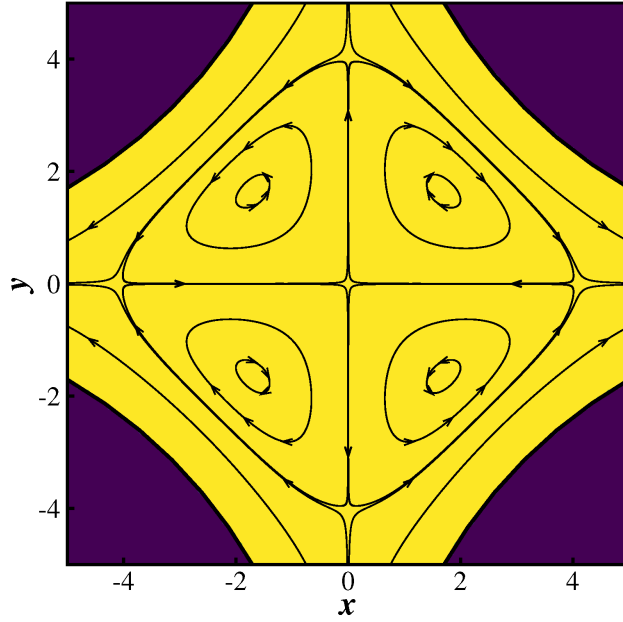


FIG. 8: Discovery of the quadrifoliate vortex mode: streamline patterns in the central region of the four-roll mill for Newtonian fluid ($n = 1$) at $Re = 10$. Four symmetrical vortices of equal size form around the stagnation point, with adjacent vortices rotating in opposite directions. The geometric parameters are set to $h = 1$, $r = 9$, and $\delta \approx 2.56$.

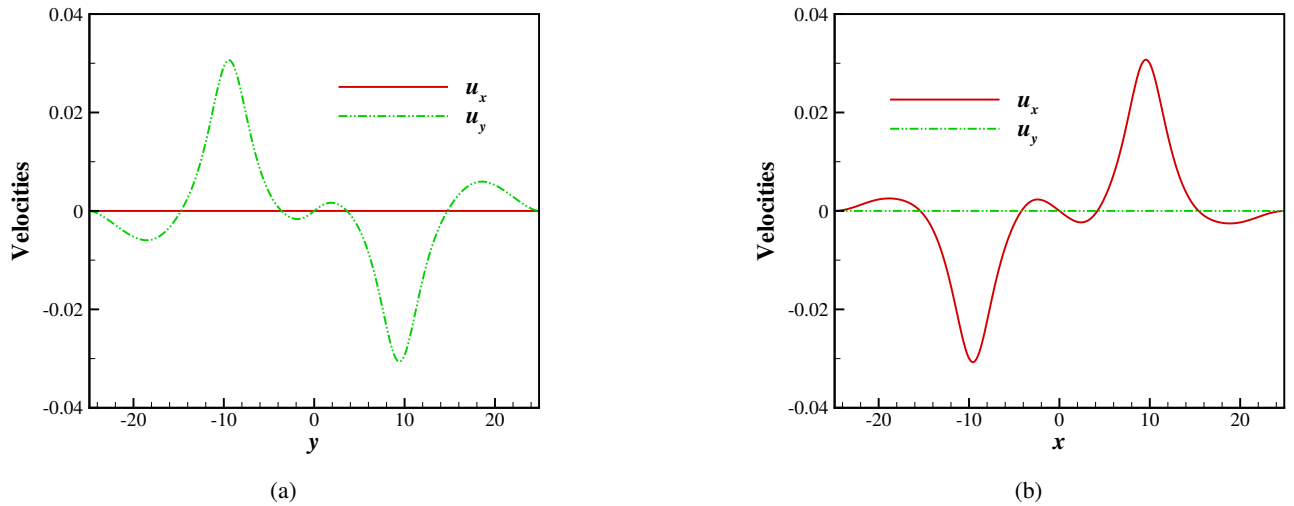


FIG. 9: Velocity distributions in the quadrifoliate vortex mode: profiles of u_x and u_y along (a) y -axis and (b) x -axis for Newtonian fluid ($n = 1$) at $Re = 10$. Geometric parameters: $h = 1$, $\delta \approx 2.56$, and $r = 9$.

be noted, however, that finer grid resolution may be required for cases with small power-law indices, where non-physical spindle-shaped streamline mode might emerge in the central region without adequate spatial resolution (this phenomenon will be discussed in detail in Section IV B).

IV. RESULTS AND DISCUSSION

This section presents a systematic investigation of flow characteristics in the four-roll mill. In Section IV A, we first analyze the flow modes of Newtonian fluids and examine how varying Reynolds numbers influence the emergence of different flow modes. Section IV B extends this analysis to power-law fluids, focusing on their distinct mode transition behaviors.

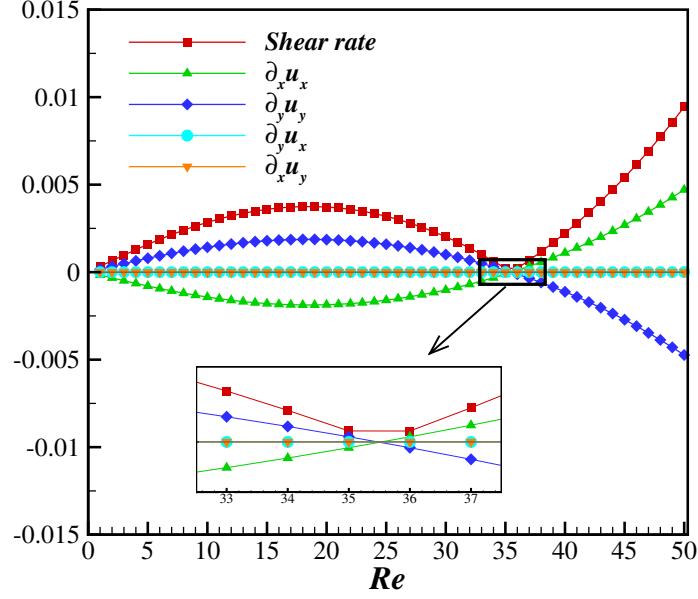


FIG. 10: Variation of shear rate and velocity gradients at point O with Reynolds number for a Newtonian fluid ($n = 1$). The geometric parameters are fixed at $h = 1$, $\delta \approx 2.56$, and $r = 9$.

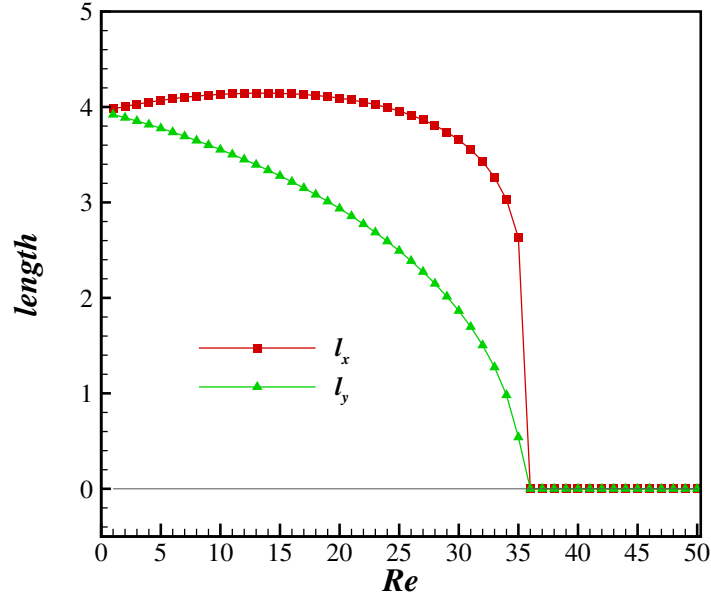


FIG. 11: Vortex dimensions (l_x and l_y) as functions of Reynolds number for Newtonian fluid ($n = 1$) with geometric parameters $h = 1$, $\delta \approx 2.56$, and $r = 9$, where l_x and l_y represent the vortex extent in the horizontal and vertical directions, respectively.

The effects of geometric parameters, specifically the roller-container gap δ and roller radius r , on flow characteristics are investigated in Section IV C.

A. Flow modes of Newtonian fluid under different Re

The geometric parameters are initially set as $r = 9$, $L_c = 50$, and $h = 1$, which determine the corresponding values of $I \approx 4.44$ and $\delta \approx 2.56$. The viscosity coefficient μ_0 is fixed at 0.002 unless otherwise specified. A series of numerical

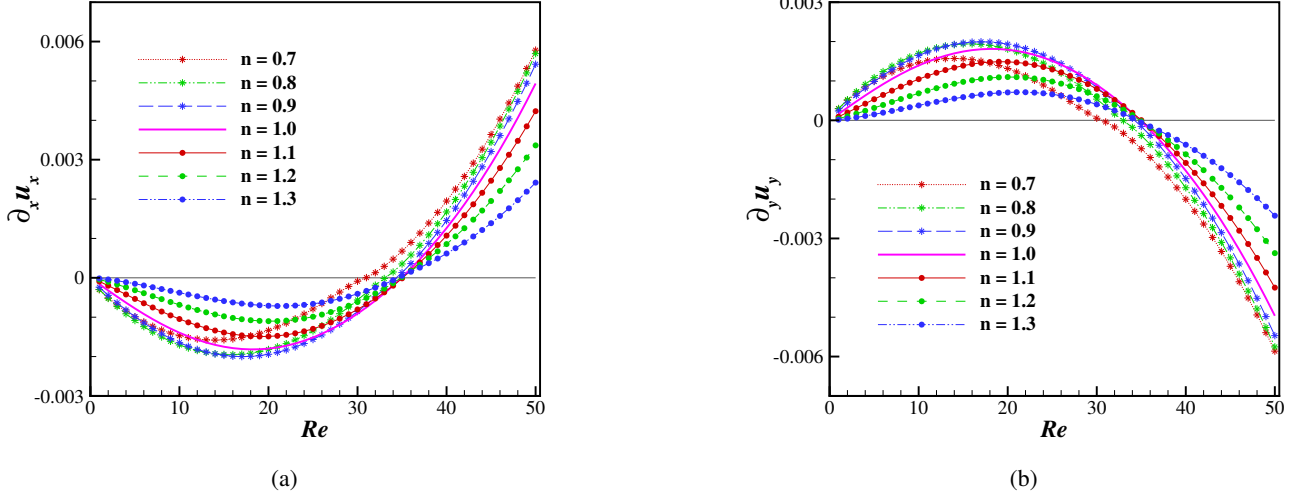


FIG. 12: Velocity gradients (a) $\partial_x u_x$ and (b) $\partial_y u_y$ at the stagnation point O plotted against Reynolds number for different power-law indices n . The geometric parameters are fixed at $h = 1$, $\delta \approx 2.56$, and $r = 9$.

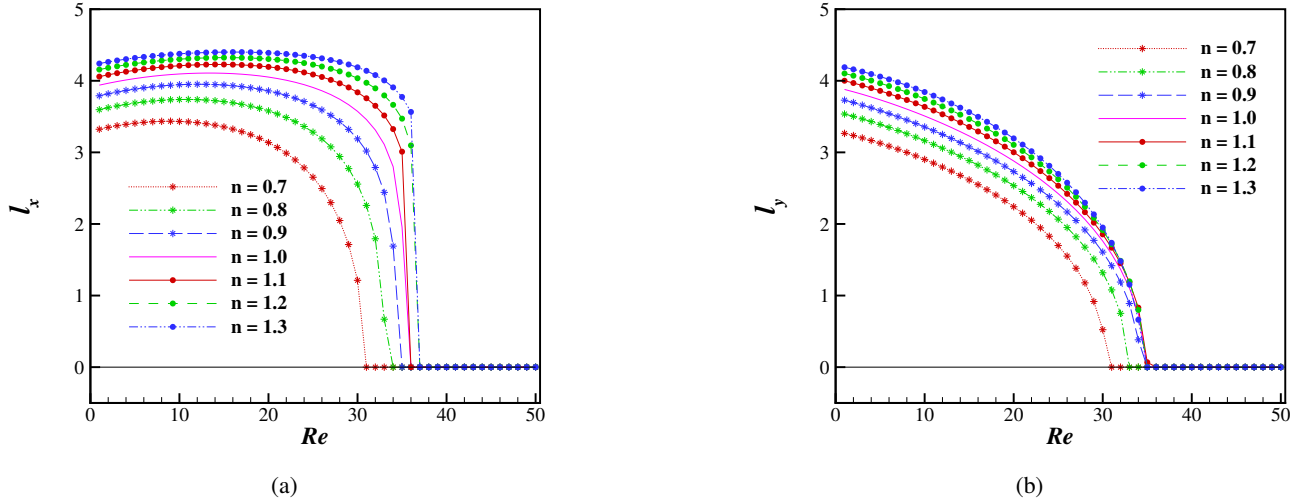


FIG. 13: Variations of vortex lengths (a) l_x and (b) l_y with Re for various values of power-law index, $h = 1$, $\delta \approx 2.56$, and $r = 9$.

simulations are performed for a Newtonian fluid ($n = 1.0$) over Reynolds numbers ranging from 1 to 50.

Fig. 6 illustrates the flow structure in the four-roll mill for Newtonian fluid at $Re = 50$ through streamline plots of (a) the entire domain and (b) the central region. Eight vortices are observed in Fig. 6a, which remain isolated from the central flow as they do not interact with the inlet and outlet of the central region. Fig. 6b demonstrates that the central region exhibits simple extensional flow, consistent with previous experimental (Taylor, 1934; Bentley and Leal, 1986) and numerical investigations (Feng and Leal, 1997) of four-roll mills. The velocity profiles u_x and u_y along the y -axis and x -axis at $Re = 50$ are presented in Fig. 7. Both velocity components vanish at point O , confirming its stagnation point nature, and exhibit central symmetry about this point. Moreover, the vanishing of u_x along

the y -axis and u_y along the x -axis indicates the absence of fluid exchange between quadrants.

At $Re = 10$, the streamline patterns in the central region exhibit a distinct flow mode, as shown in Fig. 8. Four symmetrical vortices form around point O , with adjacent vortices rotating in directions opposite to their neighboring rollers. Although these vortices dominate the central region, detailed examination reveals that the flow near point O maintains extensional characteristics, albeit with reversed directions compared to the $Re = 50$ case: the vertical direction transitions from compression to extension, while the horizontal direction shifts from extension to compression. This previously unreported flow configuration, which we term the quadrifoliate vortex mode due to its four-leaf pattern, represents a novel finding in four-roll mill dynamics.

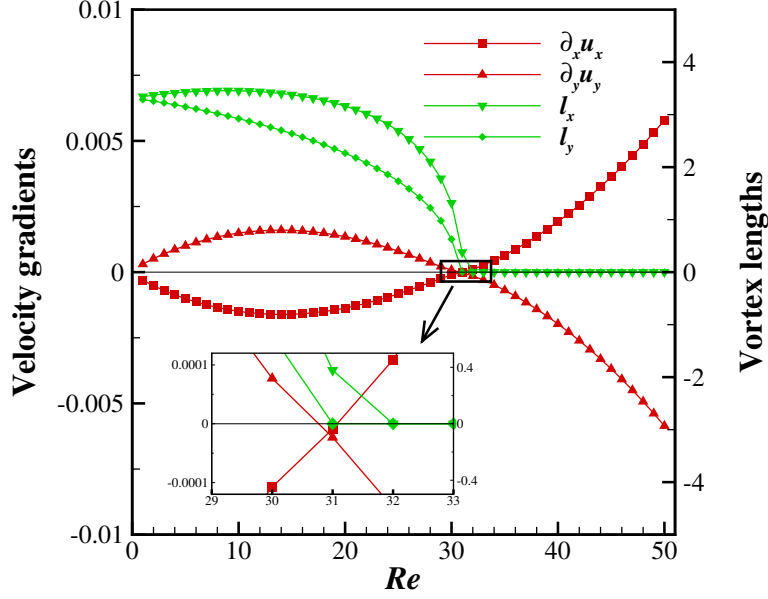


FIG. 14: Variations of velocity gradients and vortex lengths with Re for $n = 0.7$.

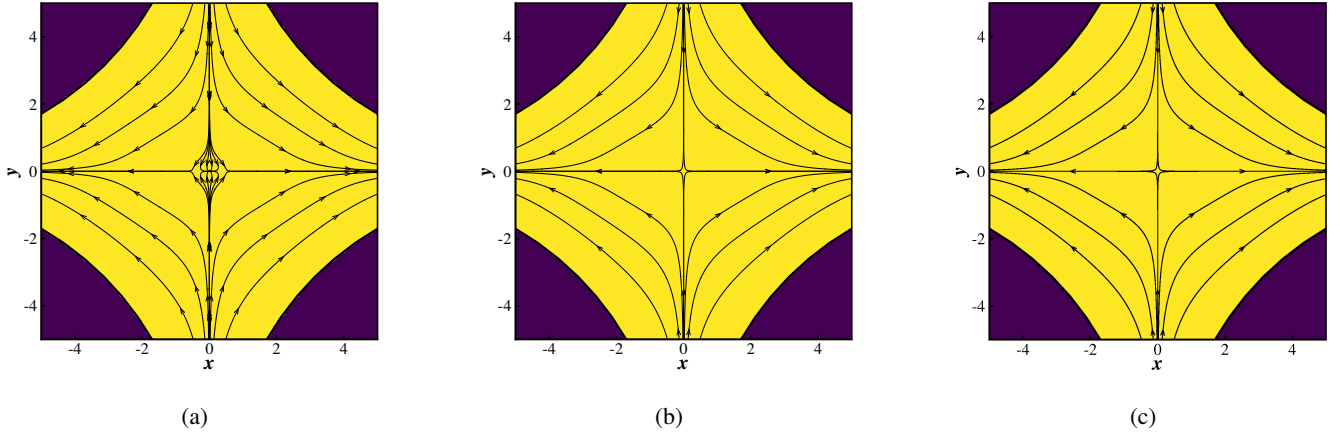


FIG. 15: Central streamline in the four roll mill for $n = 0.7$, $Re = 31$, $h = 1$, $\delta \approx 2.56$, and $r = 9$ under different meshes including (a) 800×800 , (b) 1600×1600 , and (c) 3200×3200 .

The velocity profiles at $Re = 10$, presented in Fig. 9, share certain characteristics with the simple extensional flow: both u_x along the y -axis and u_y along the x -axis vanish, indicating no cross-axial fluid transport. As shown in Fig. 9a, u_y reaches its maximum at the inlet ($y = -9.5$) due to the local flow constriction. The velocity u_y exhibits a characteristic evolution from inlet to point O : it initially decreases to zero, reaches a minimum value, and finally returns to zero. The position where u_y first vanishes defines the vortex generation point, with the vortex length l_y measured as the distance from this point to point O . Similar velocity characteristics and vortex length definition (l_x) apply along the x -axis, as demonstrated in Fig. 9b.

Comparing the cases of $Re = 10$ and $Re = 50$, it is evident

that a reduction in the roller speed leads to the emergence of vortices in the central region of the flow field under the same structure and fluid. Additionally, the original vertical compression transforms into extension, and the horizontal extension becomes compression at point O . The states of compression and extension at point O can be quantified using $\partial_x u_x$ and $\partial_y u_y$. These gradients, computed via the second-order central differencing, indicate the magnitude and direction of compression or extension at point O . Specifically, if $\partial_y u_y > 0$, it indicates extension in the vertical direction at point O ; if $\partial_y u_y < 0$, it indicates compression. The same interpretation applies to $\partial_x u_x$ for the horizontal direction.

Fig. 10 depicts the evolution of shear rate and velocity gradients at point O with varying Re . The velocity gradients $\partial_x u_y$

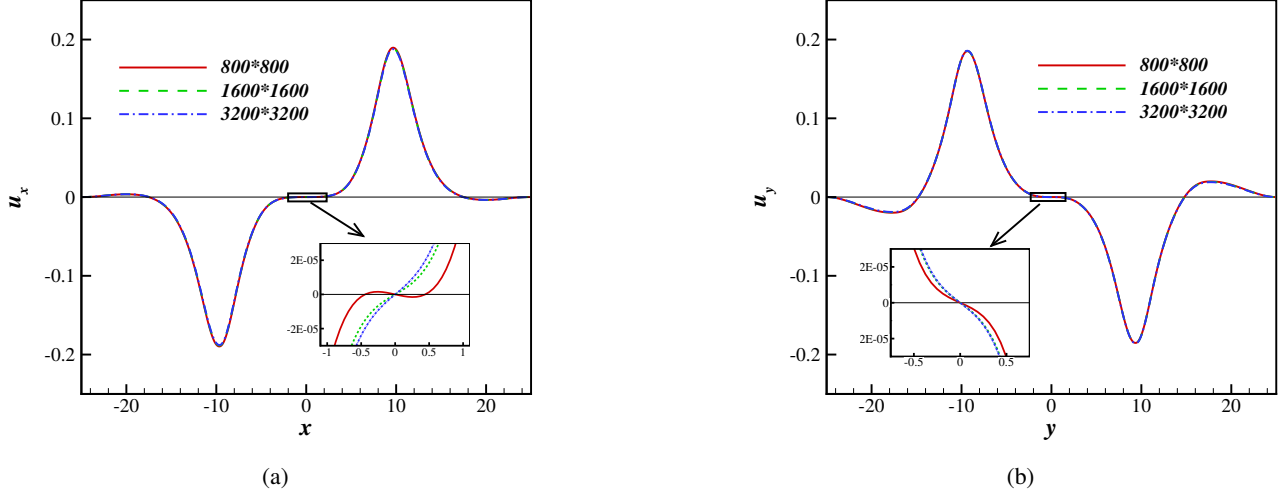


FIG. 16: The velocity profiles (a) u_x in x -axis and (b) u_y in y -axis for $n = 0.7$, $Re = 31$, $h = 1$, $\delta \approx 2.56$, and $r = 9$ under different meshes.

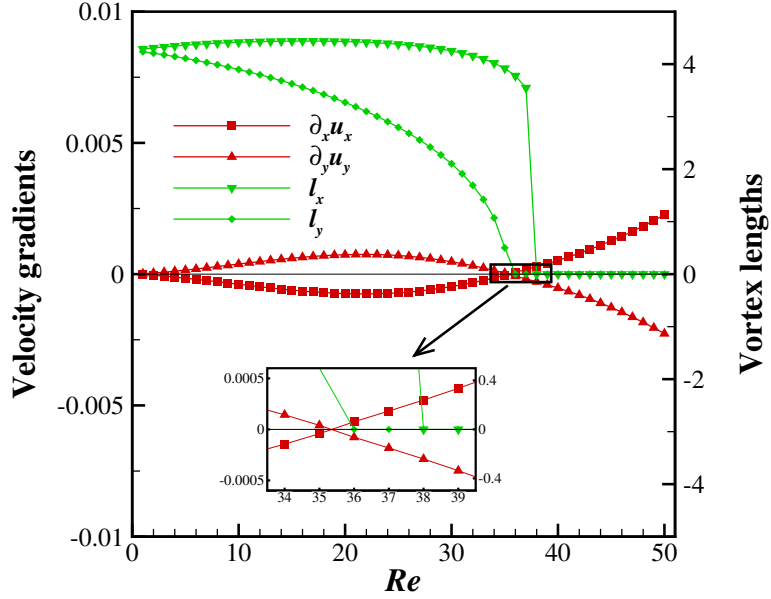


FIG. 17: Variations of velocity gradients and vortex lengths with Re for $n = 1.3$.

and $\partial_y u_x$ consistently remain zero, confirming the absence of cross-axial fluid transport. Consequently, the shear rate is determined solely by $\partial_x u_x$ and $\partial_y u_y$. A critical transition is observed between $Re = 35$ and $Re = 36$, where $\partial_x u_x$ and $\partial_y u_y$ undergo sign reversal. This marks the transition from the quadrifoliate vortex mode ($\partial_x u_x > 0$ and $\partial_y u_y < 0$) to simple extensional flow ($\partial_x u_x < 0$ and $\partial_y u_y > 0$). For $Re \geq 36$, the flow maintains simple extensional characteristics. This transition point defines the critical Reynolds number Re_c , which equals 36 under the current configuration.

The evolution of vortex dimensions with Reynolds number

is characterized through the lengths l_x and l_y . Given the symmetry of the four vortices, we focus on the size variation of a single vortex. Fig. 11 illustrates the variation of l_x and l_y over Re ranging from 1 to 50. Both lengths exhibit monotonic decrease with increasing Re , eventually vanishing at $Re = 36$. This point marks the disappearance of the quadrifoliate vortex mode and its transition to simple extensional flow. Notably, throughout the quadrifoliate vortex regime, l_x consistently exceeds l_y . These observations establish that the critical Reynolds number Re_c can be determined through two independent criteria: the reversal of velocity gradients ($\partial_x u_x$ and $\partial_y u_y$) and the

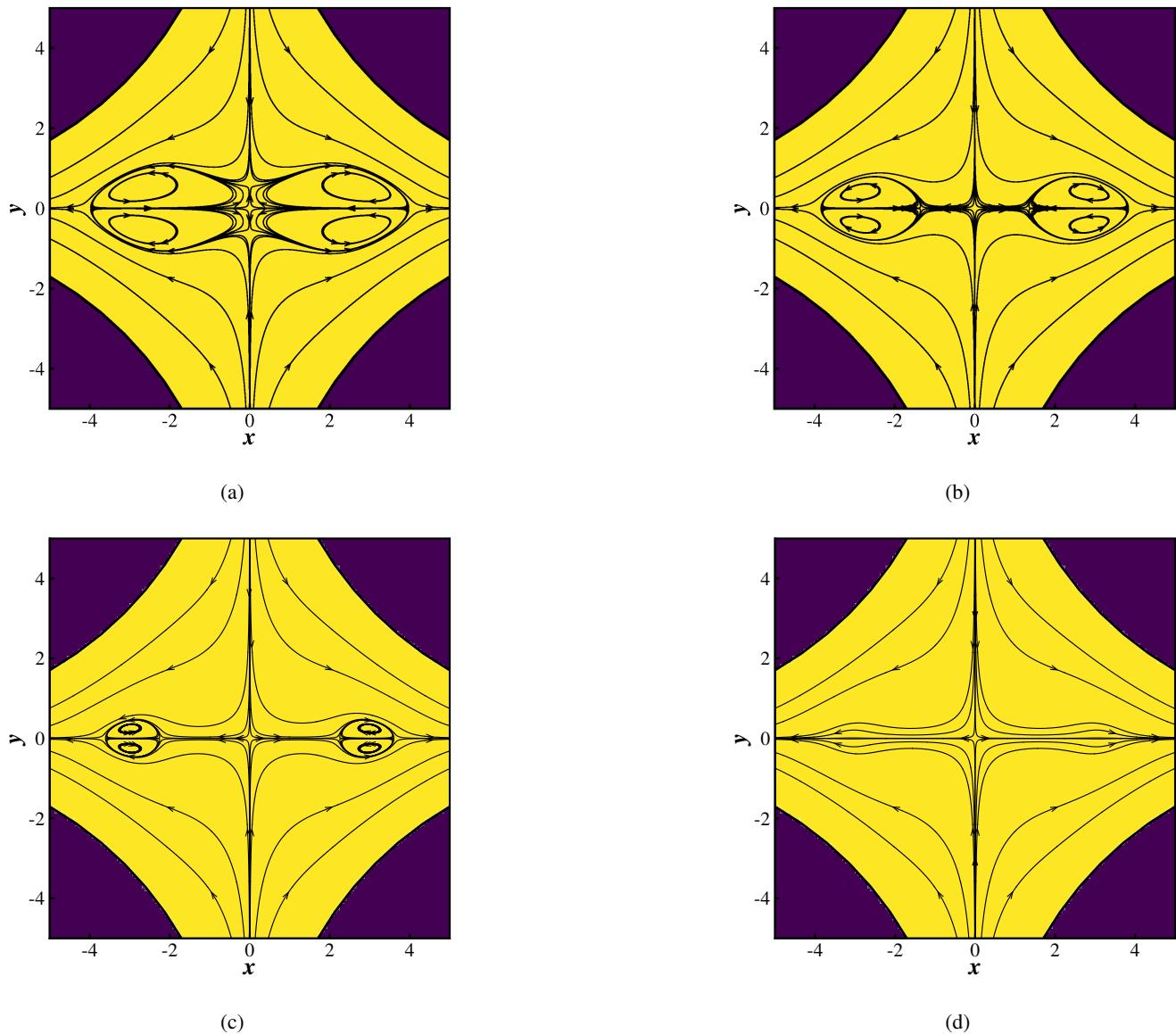


FIG. 18: Central streamline in the four roll mill at (a) $Re = 35$, (b) $Re = 36$, (c) $Re = 37$, and (d) $Re = 38$ for $n = 1.3$, $h = 1$, $\delta \approx 2.56$, and $r = 9$ under the mesh of 800×800 .

vanishing of vortex lengths (l_x and l_y).

B. Effect of the power-law fluid

This section investigates how power-law fluids influence the flow modes in the central region, maintaining the geometric configuration described in Section IV A. The analysis spans Reynolds numbers from 1 to 50 and power-law indices from 0.7 to 1.3, encompassing both shear-thinning and shear-thickening fluid behaviors.

Fig. 12 depicts the evolution of velocity gradients $\partial_x u_x$ and $\partial_y u_y$ across the specified ranges of n and Re . For each power-law index, $\partial_x u_x$ exhibits a non-monotonic trend with increasing

Re , first decreasing then increasing, while $\partial_y u_y$ shows the opposite behavior. As illustrated in Fig. 13, throughout the range $0.7 \leq n \leq 1.3$, both vortex lengths l_x and l_y monotonically decrease to zero with increasing Re and remain zero thereafter. These characteristics mirror those observed for Newtonian fluids in Section IV A, indicating a consistent transition mechanism from the quadrifoliate vortex mode to simple extensional flow.

However, numerical complexities arise near the critical Reynolds number, where discrepancies emerge between transition points identified by velocity gradients and vortex lengths. For instance, at $n = 0.7$ (Fig. 14), the critical Re values determined from $\partial_x u_x$, $\partial_y u_y$, l_x , and l_y are 32, 31, 32, and 31, respectively. At $Re = 31$, the flow field exhibits an anomalous behavior where both $\partial_x u_x$ and $\partial_y u_y$ are negative, suggesting

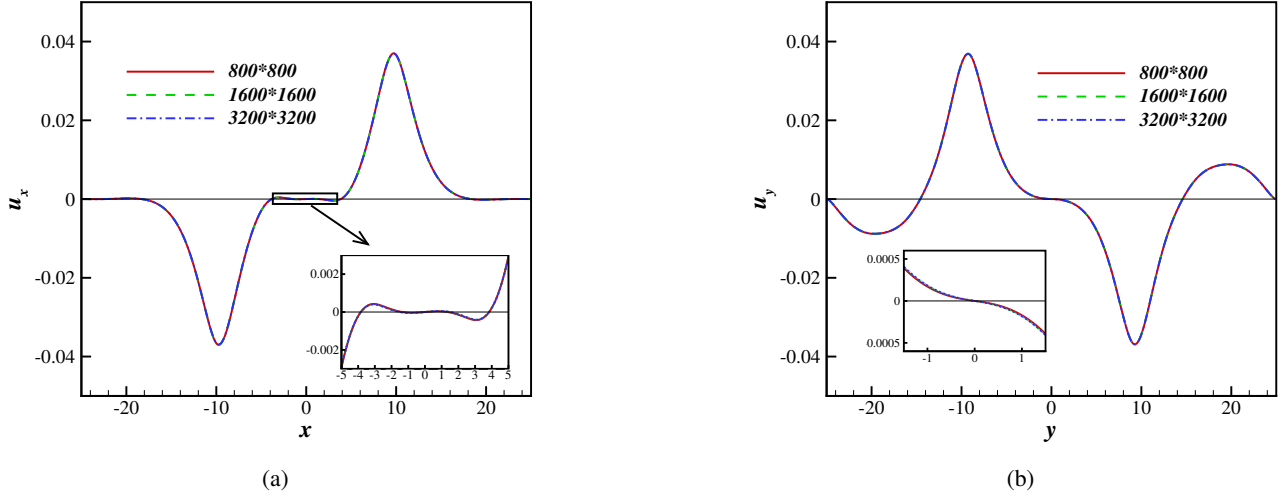


FIG. 19: The velocity profiles (a) u_x in x-axis and (b) u_y in y-axis for $n = 1.3$, $Re = 36$, $h = 1$, $\delta \approx 2.56$, and $r = 9$ under different meshes.

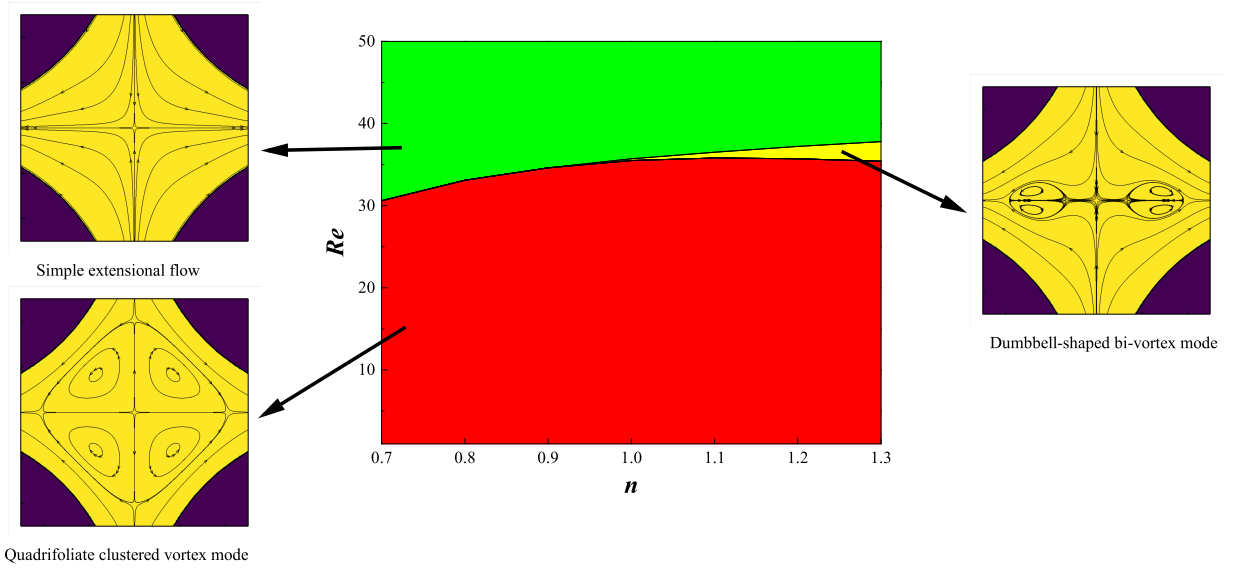


FIG. 20: A phase diagram that illustrates the different flow modes in simulation of the four-roll mill as a function of power-law index n and Reynolds number Re , with parameters $h = 1$, $\delta \approx 2.56$, and $r = 9$.

physically impossible flow convergence toward point O in both directions (Fig. 15a). This non-physical behavior is attributed to insufficient spatial resolution and can be eliminated by grid refinement. As demonstrated in Fig. 15, increasing the grid resolution to 1600×1600 and 3200×3200 resolves this anomaly. Fig. 16 compares velocity profiles under different grid resolutions, revealing that while the overall velocity distributions remain consistent, the local $\partial_x u_x$ at point O transitions from negative to positive with increasing resolution, while

$\partial_y u_y$ remains relatively unchanged. This grid-dependent behavior occurs for $0.7 \leq n \leq 0.9$ and can be effectively addressed through mesh refinement.

A distinct transition phenomenon emerges for power-law indices between 1.0 and 1.3. Taking $n = 1.3$ as a representative case, the critical Reynolds numbers determined from $\partial_x u_x$, $\partial_y u_y$, l_x , and l_y are 36, 36, 38, and 36, respectively. Fig. 17 illustrates the evolution of velocity gradients and vortex lengths with increasing Re for $n = 1.3$. At $Re = 35$ and 36, while

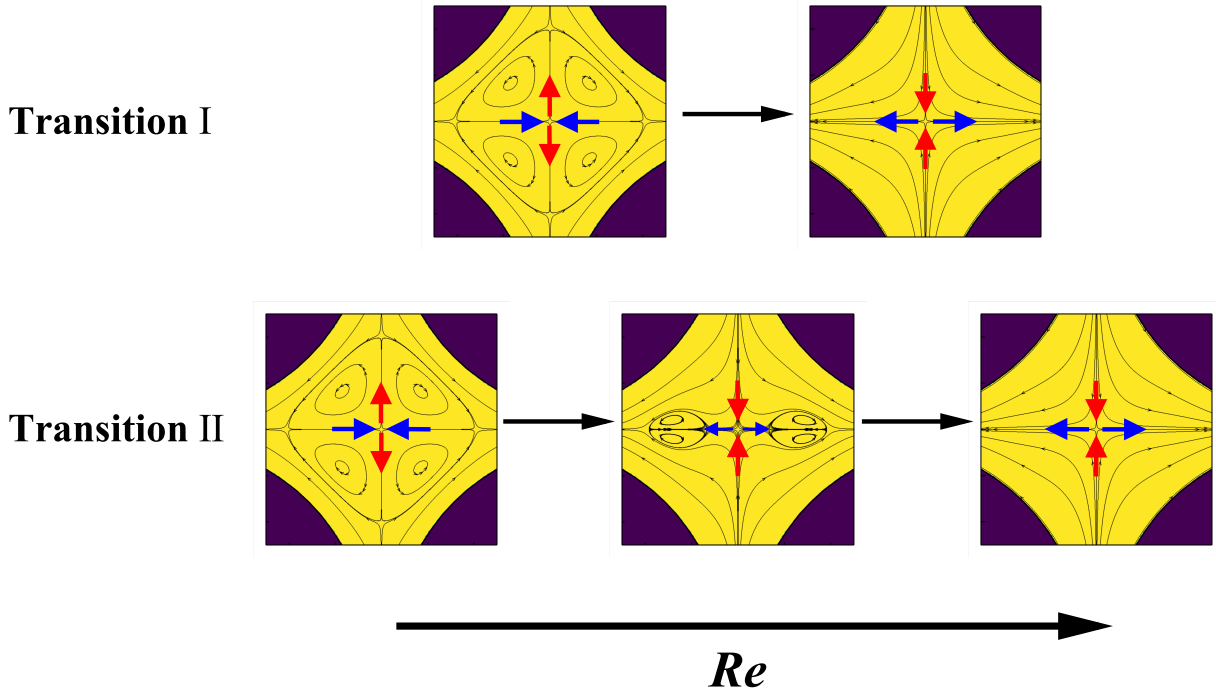


FIG. 21: Schematic representation of two distinct transition pathways in the four-roll mill. (a) Transition I: direct transformation from quadrifoliate vortex mode to simple extensional flow, typically observed at relatively small power-law indices. (b) Transition II: evolution from quadrifoliate vortex mode through an intermediate dumbbell-shaped quad-vortex mode to simple extensional flow, characteristic of relatively large power-law indices.

the velocity gradients ($\partial_x u_x < 0$ and $\partial_y u_y > 0$) exhibit characteristics of simple extensional flow, an asymmetry in vortex extinction is observed: l_y vanishes while l_x remains finite. The flow field evolution for Re ranging from 35 to 38 at $n = 1.3$ is presented in Fig. 18. The flow transitions from a well-defined quadrifoliate vortex mode at $Re = 35$ to simple extensional flow at $Re = 38$. However, at intermediate Reynolds numbers ($Re = 36$ and 37), a previously unreported flow configuration emerges, distinctly different from the anomalous behavior observed in Fig. 15a. This intermediate state is characterized by four vortices symmetrically attached to the x -axis and displaced laterally from point O . As Re increases from 36 to 37, these vortices progressively shrink before completely disappearing at $Re = 38$, giving way to simple extensional flow. Grid independence analysis confirms the physical nature of this phenomenon. Fig. 19 demonstrates that velocity profiles along both axes remain consistent across different grid resolutions, with the stagnation points associated with the four vortices maintaining their positions along the x -axis. This intermediate flow configuration, observed for power-law indices from 1.0 to 1.3, serves as a transitional state between the quadrifoliate vortex mode and simple extensional flow. Due to its characteristic shape, we designate this newly identified flow state as the

dumbbell-shaped quad-vortex mode.

Based on the above findings, we have identified two previously unreported flow modes in the four-roll mill: the quadrifoliate vortex mode and the dumbbell-shaped quad-vortex mode. To systematically characterize these flow modes and their transitions, we present a comprehensive phase diagram in Fig. 20, mapping the flow regimes as functions of power-law index n and Reynolds number Re . The diagram is constructed with refined resolution ($\Delta Re = 0.1$) near critical transitions and coarser resolution ($\Delta Re = 1$) elsewhere. The phase diagram reveals two distinct transition pathways depending on the power-law index: For shear-thinning fluids ($0.7 \leq n < 1.0$), increasing Re triggers a direct transition from the quadrifoliate vortex mode to simple extensional flow, with the transition Reynolds number increasing monotonically with n . In contrast, shear-thickening fluids ($1.0 \leq n \leq 1.3$) exhibit a more complex behavior, where the dumbbell-shaped quad-vortex mode emerges as an intermediate state. The critical Re for the initial transition (quadrifoliate to dumbbell-shaped) shows a non-monotonic dependence on n , while the subsequent transition (dumbbell-shaped to simple extensional) occurs at progressively higher Re as n increases. Furthermore, the dumbbell-shaped quad-vortex mode becomes increasingly prevalent at higher power-law indices.

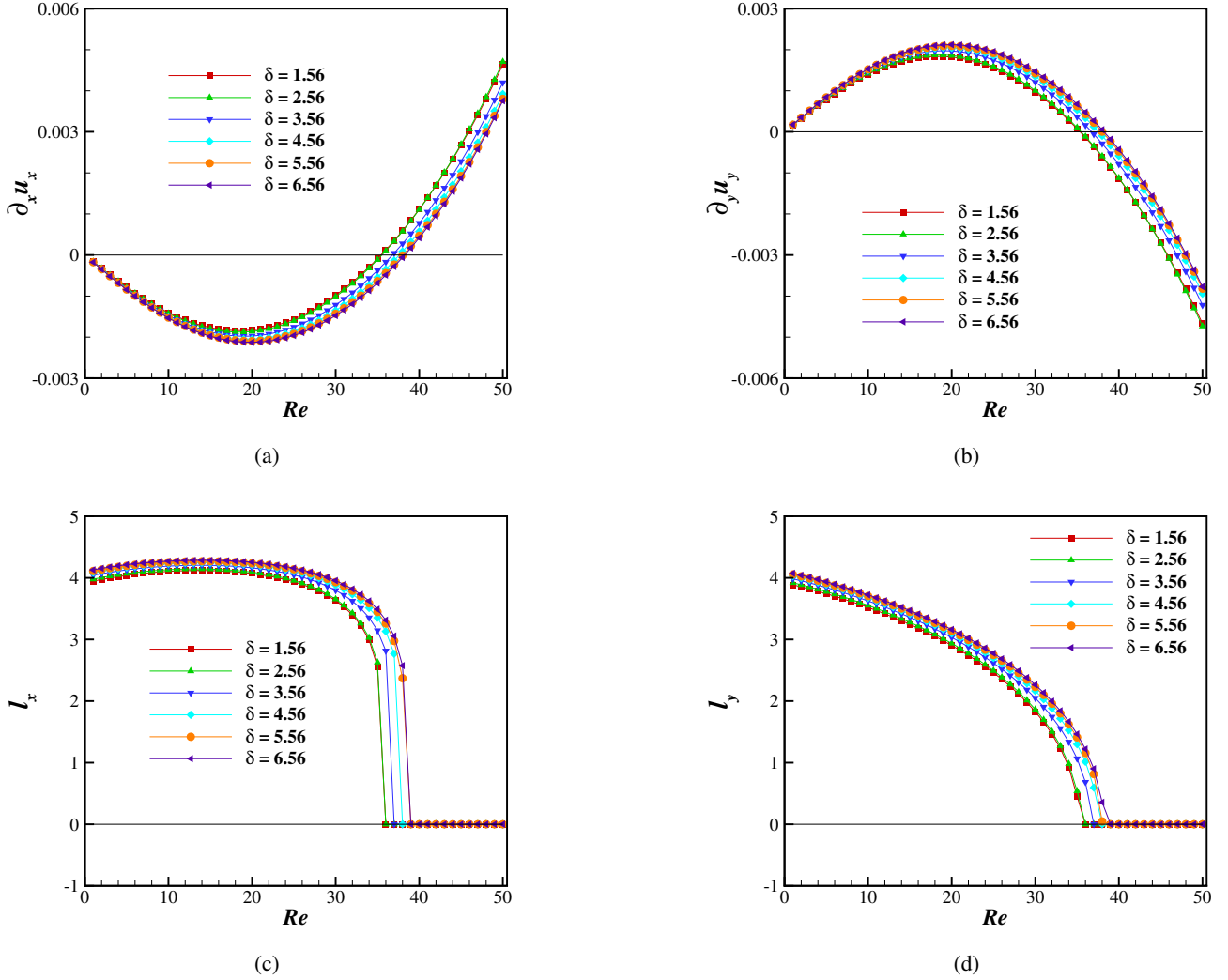


FIG. 22: Variation of velocity gradients (a) $\partial u_x/\partial x$, (b) $\partial u_y/\partial y$ at point O and vortex lengths (c) l_x , and (d) l_y with Re for δ values of 1.56, 2.56, 3.56, 4.56, 5.56, and 6.56, with parameters $h = 1$ and $r = 9$.

dices, with its stability range expanding with increasing n . These distinct transition scenarios are schematically illustrated in Fig. 21.

C. Effect of geometric configuration in four-roll mill

Having characterized the flow modes and their transitions for a specific geometry, we now investigate how the geometric parameters of the four-roll mill influence these phenomena. Our analysis focuses on two key geometric parameters: the roller radius r and the roller-container gap δ . The investigation spans Reynolds numbers from 1 to 50 and power-law indices from 0.7 to 1.3, enabling a systematic comparison of flow modes in the central region across different geometric configurations.

1. The gap δ between the rollers and the container

To examine how the outer region beyond the four rollers influences the central flow modes, we maintained fixed values of $h = 1$ and $r = 9$ while systematically varying δ . The container diameter L_c was set to 48, 50, 52, 54, 56, and 58, yielding corresponding δ values of 1.56, 2.56, 3.56, 4.56, 5.56, and 6.56.

Fig. 22 presents the Reynolds number dependence of (a) $\partial u_x/\partial x$, (b) $\partial u_y/\partial y$ at point O , and vortex lengths (c) l_x and (d) l_y for a Newtonian fluid across different δ values. These parameters exhibit evolution patterns consistent with our earlier observations: $\partial u_x/\partial x$ shows an initial decrease followed by an increase, while $\partial u_y/\partial y$ displays the opposite trend. Both l_x and l_y monotonically decrease to zero and remain there. For each δ , the critical Reynolds numbers Re_c derived from different criteria coincide, indicating that only the extensional flow and quadrifoliate vortex mode exist within this Re range. The effect

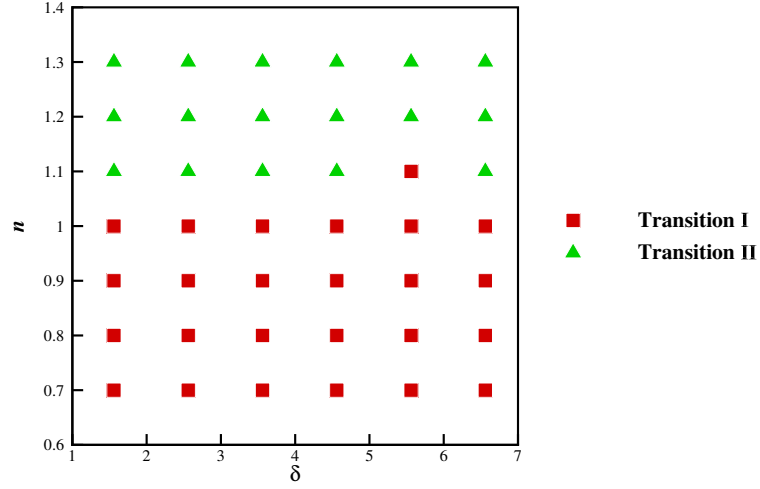


FIG. 23: A phase diagram that illustrates the different mode transitions at $h = 1$ and $r = 9$ for δ values of 1.56, 2.56, 3.56, 4.56, 5.56, and 6.56 and n ranging from 0.7 to 1.3.

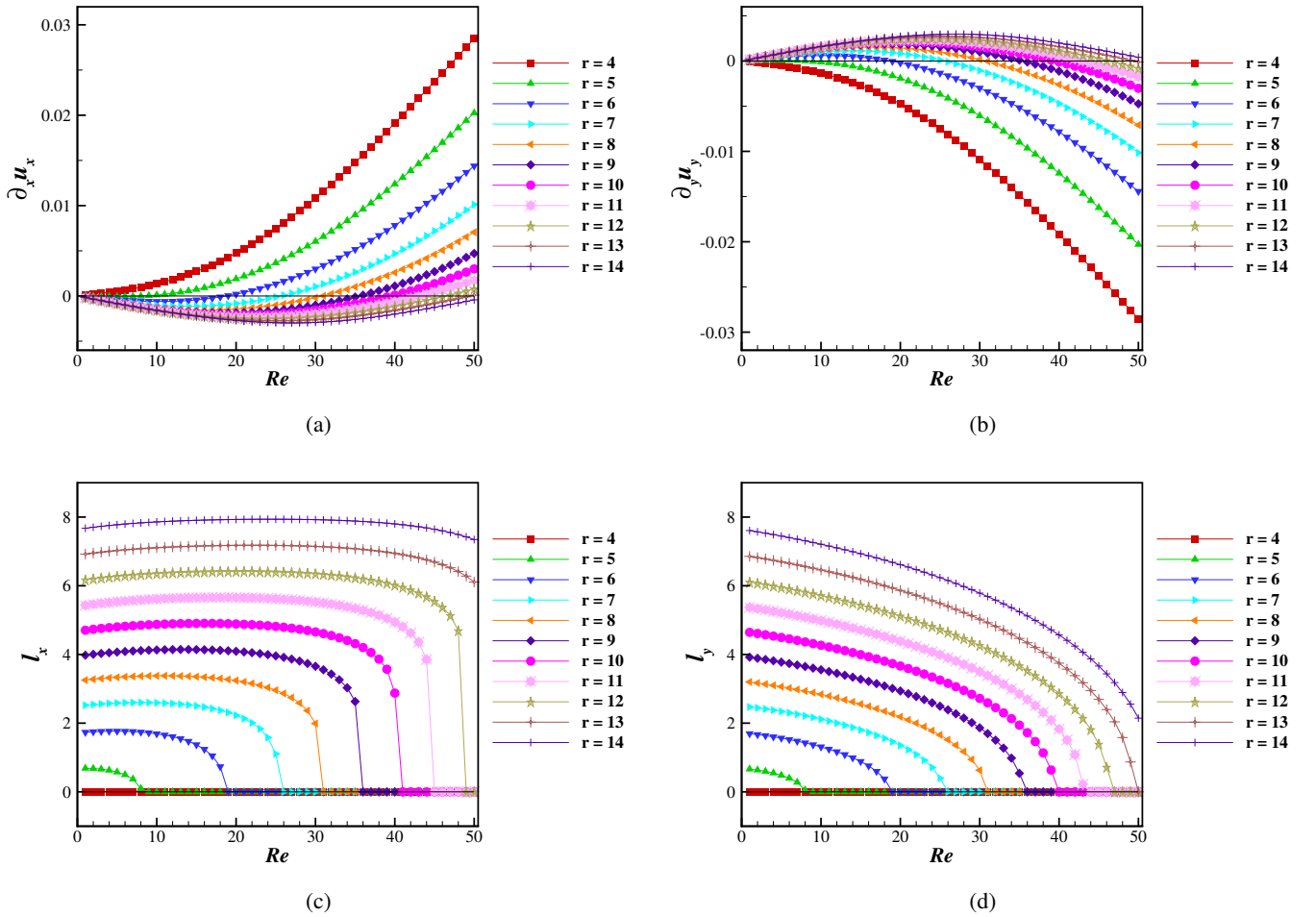


FIG. 24: Variations of velocity gradients (a) $\partial u_x / \partial x$, (b) $\partial u_y / \partial y$ at point O and vortex lengths (c) l_x and (d) l_y with Re for r values from 4 to 14, with parameters $h = 1$ and $\delta \approx 2.56$.

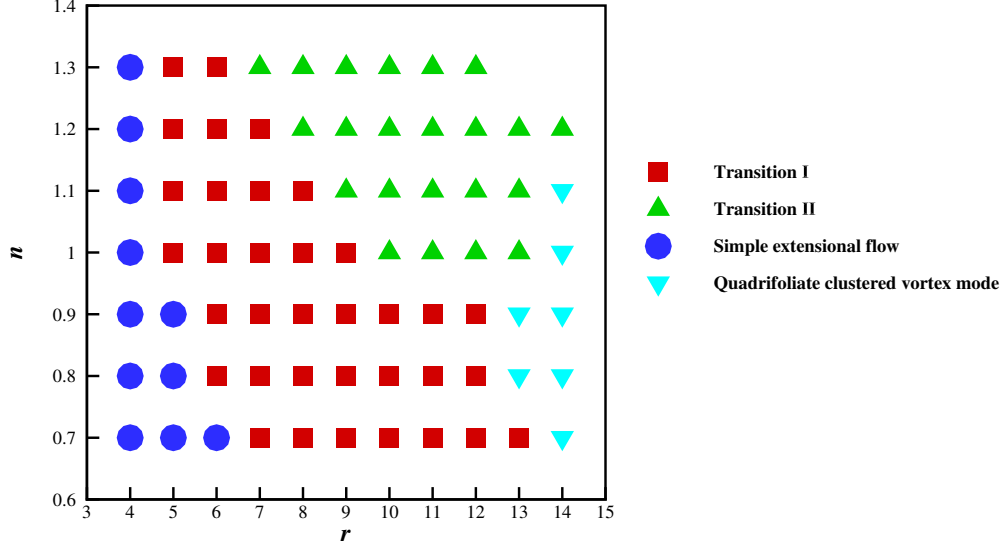


FIG. 25: A phase diagram that illustrates the different mode transitions at $h = 1$ and $\delta \approx 2.56$ for r ranging from 4 to 14 and n from 0.7 to 1.3.

of varying δ manifests primarily in the magnitude of these parameters: at fixed Re , increasing δ leads to decreased $\partial u_x/\partial x$, increased $\partial u_y/\partial y$, and slightly enlarged vortex dimensions in the quadrifoliate mode.

Fig. 23 illustrates the two transition types across different δ values and power-law indices. For each δ , both transition mechanisms are observed across the range $0.7 \leq n \leq 1.3$, with Transition I predominating near $n = 0.7$ and Transition II near $n = 1.3$. Notably, the transition characteristics remain largely invariant across different δ values at fixed n .

2. The roller radius r

To examine the influence of roller radius on flow characteristics, we investigated configurations with fixed $\delta = 2.56$ and $h = 1$ while varying r from 4 to 14.

Fig. 24 presents the evolution of velocity gradients ($\partial u_x/\partial x$, $\partial u_y/\partial y$) and vortex lengths (l_x , l_y) for a Newtonian fluid across Reynolds numbers from 1 to 50. For roller radii between 5 and 12, these parameters exhibit familiar trends: $\partial u_x/\partial x$ shows an initial decrease followed by an increase, while $\partial u_y/\partial y$ displays the opposite behavior. Both vortex lengths monotonically decrease to zero. However, distinct behavior emerges at larger roller radii. At $r = 13$, while l_y vanishes and both velocity gradients reverse sign at $Re = 50$, l_x remains finite, suggesting $Re_c > 50$. This behavior mirrors Transition II described in Fig. 21. For $r = 14$, both vortex lengths remain non-zero, indicating persistent quadrifoliate vortex mode throughout the examined Reynolds number range. At fixed Re , increasing r enhances $\partial u_y/\partial y$ and both vortex lengths while reducing $\partial u_x/\partial x$. Notably, when present, the vortex dimensions scale nearly linearly with roller radius at constant Re .

Fig. 25 maps the flow behavior across different values of r and n . As Re increases from 1 to 50, we observe four distinct flow scenarios: two transition processes and two stable modes (simple extensional flow and quadrifoliate vortex mode without transitions). The transition processes correspond to those shown in Fig. 21. Cases for $n = 1.3$ and $r = 13, 14$ are excluded due to numerical convergence issues. Notably, at $r = 4$, only simple extensional flow is observed across all power-law indices, consistent with previous findings in the literature. Clear patterns emerge in the parameter space: when $r < 7$ and $n < 1.0$, the flow tends to maintain simple extensional characteristics; conversely, near $r = 14$, the flow preferentially remains in the dumbbell-shaped quad-vortex mode. Transition II predominantly occurs in regions where $n > 1.0$ and $r > 7$, while Transition I appears in the intermediate regions between Transition II and the stable modes.

V. CONCLUSION

We have conducted systematic numerical investigations of flow characteristics in the central region of a four-roll mill containing Newtonian or power-law fluids. The simulations employed a two-relaxation-time regularized lattice Boltzmann model, representing the first successful extension of this methodology to power-law fluid dynamics with curved boundaries. After validating our numerical framework against canonical test cases, we discovered and characterized two previously unreported flow modes and their supercritical bifurcation transitions. Our parameter space investigation spans Reynolds numbers ($1 \leq Re \leq 50$), power-law indices ($0.7 \leq n \leq 1.3$), and geometric configurations. The key findings are:

- (a) The central region of the four-roll mill exhibits a novel

quadrifoliate vortex mode at low Reynolds numbers, characterized by four symmetrical vortices with alternating rotation directions. As Re increases, these vortices progressively shrink and eventually vanish, transitioning to simple extensional flow. This transition is accompanied by a reversal in the local deformation pattern at the stagnation point, where the flow switches from horizontal compression/vertical extension to horizontal extension/vertical compression.

- (b) The transition from quadrifoliate vortex mode to simple extensional flow follows two distinct pathways depending on the power-law index. At relatively small power-law indices, a direct transition occurs (Transition I). In contrast, at relatively large power-law indices, the transition proceeds through an intermediate dumbbell-shaped quad-vortex mode (Transition II), where vortices detach from the stagnation point while maintaining their presence along the horizontal axis.
- (c) These transition mechanisms can be quantitatively characterized through multiple bifurcation criteria. In Transition I, all characteristic parameters ($\partial u_x/\partial x$, $\partial u_y/\partial y$, l_x , and l_y) yield identical critical Reynolds numbers. Transition II shows a distinctive signature where l_x persists beyond the critical point indicated by other parameters, reflecting the unique spatial structure of the dumbbell-shaped mode.
- (d) The geometric parameters exhibit markedly different effects on flow structures. While the roller-container gap δ has minimal influence on flow transitions and vortex dimensions, the roller radius r emerges as a crucial parameter. Larger r values not only lead to proportionally larger vortices but can also fundamentally alter the transition pathways, with sufficiently large radii stabilizing the quadrifoliate vortex mode even at high Reynolds numbers.

These findings significantly advance our understanding of flow physics in four-roll mills and provide practical guidance for achieving desired flow patterns in applications. The identification of supercritical bifurcations and distinct transition pathways offers new opportunities for flow control and optimization in extensional devices. Future work should explore the stability characteristics of these newly discovered flow modes and investigate their potential applications in material processing and rheological measurements.

ACKNOWLEDGEMENTS.

This research was supported in part by the High Performance Computing Platform of Xiangtan University. The authors gratefully acknowledge this computational resource that enabled the detailed numerical investigations presented in this work.

FUNDING.

This work is financially supported by the National Natural Science Foundation of China (Grant Nos. 12101527, 12271464 and 11971414), the Science and Technology Innovation Program of Hunan Province (Program No. 2021RC2096), Project of Scientific Research Fund of Hunan Provincial Science and Technology Department (Grant No. 21B0159) and the Natural Science Foundation for Distinguished Young Scholars of Hunan Province (Grant No. 2023JJ10038).

DECLARATION OF INTERESTS.

The authors report no conflict of interest.

- Akbaridoust, F., Philip, J., and Marusic, I., "Assessment of a miniature four-roll mill and a cross-slot microchannel for high-strain-rate stagnation point flows," *Measurement Science and Technology* **29**, 045302 (2018).
- Andreotti, B., Douady, S., and Couder, Y., "An experiment on two aspects of the interaction between strain and vorticity," *Journal of Fluid Mechanics* **444**, 151–174 (2001).
- Arratia, P. E., Thomas, C. C., Diorio, J., and Gollub, J. P., "Elastic instabilities of polymer solutions in cross-channel flow," *Phys. Rev. Lett.* **96**, 144502 (2006).
- Balasuriya, S. and Padberg-Gehle, K., "Controlling the Unsteady Analogue of Saddle Stagnation Points," *SIAM Journal on Applied Mathematics* **73**, 1038–1057 (2013).
- Bentley, B., *Drop Deformation and Burst in Two-Dimensional Flows*, Ph.D. thesis, California Institute of Technology (1985).
- Bentley, B. J. and Leal, L. G., "A computer-controlled four-roll mill for investigations of particle and drop dynamics in two-dimensional linear shear flows," *Journal of Fluid Mechanics* **167**, 219 (1986).
- Bryngelson, S. H. and Freund, J. B., "Non-modal floquet stability of capsules in large-amplitude oscillatory extensional flow," *European Journal of Mechanics - B/Fluids* **77**, 171–176 (2019).
- Crowley, D. G., Frank, F. C., Mackley, M. R., and Stephenson, R. G., "Localized flow birefringence of polyethylene oxide solutions in a four roll mill," *Journal of Polymer Science: Polymer Physics Edition* **14**, 1111–1119 (1976).
- D'Avino, G. and Maffettone, P. L., "Numerical simulations of dispersive mixing of viscoelastic suspensions in a four-roll mill," *Rheologica Acta* **56**, 695–706 (2017).
- Dunlap, P. and Leal, L., "Dilute polystyrene solutions in extensional flows: Birefringence and flow modification," *Journal of Non-Newtonian Fluid Mechanics* **23**, 5–48 (1987).
- Feng, J. and Leal, L., "Numerical simulations of the flow of dilute polymer solutions in a four-roll mill," *Journal of Non-Newtonian Fluid Mechanics* **72**, 187–218 (1997).
- Fuller, G. G. and Leal, L. G., "Flow birefringence of dilute polymer solutions in two-dimensional flows," *Rheologica Acta* **19**, 580–600 (1980).
- Fuller, G. G. and Leal, L. G., "Flow birefringence of concentrated polymer solutions in two-dimensional flows," *Journal of Polymer Science: Polymer Physics Edition* **19**, 557–587 (1981).
- Ginzburg, I., Verhaeghe, F., and d'Humières, D., "Two-relaxation-time lattice boltzmann scheme: About parametrization, velocity, pressure and mixed boundary conditions," *Communications in Computational Physics* **3**, 427–478 (2008).
- Ha, J.-W. and Leal, L. G., "An experimental study of drop deformation and breakup in extensional flow at high capillary number," *Physics of Fluids* **13**, 1568–1576 (2001).
- Haward, S. J., McKinley, G. H., and Shen, A. Q., "Elastic instabilities in planar elongational flow of monodisperse polymer solutions," *Scientific Reports* **6**, 33029 (2016).
- Haward, S. J., Ober, T. J., Oliveira, M. S. A., Alves, M. A., and McKinley, G. H., "Extensional rheology and elastic instabilities of a wormlike micel-

- lar solution in a microfluidic cross-slot device.” *Soft Matter* **8**, 536–555 (2012a).
- Haward, S. J., Oliveira, M. S. A., Alves, M. A., and McKinley, G. H., “Optimized cross-slot flow geometry for microfluidic extensional rheometry.” *Physical review letters* **109** **12**, 128301 (2012b).
- Higdon, J. J. L., “The kinematics of the four-roll mill.” *Physics of Fluids A: Fluid Dynamics* **5**, 274–276 (1993).
- Hsiao, K.-W., Sasmal, C., Ravi Prakash, J., and Schroeder, C. M., “Direct observation of DNA dynamics in semidilute solutions in extensional flow,” *Journal of Rheology* **61**, 151–167 (2016).
- Hymel, S. J., Lan, H., and Khismatullin, D. B., “Elongation index as a sensitive measure of cell deformation in high-throughput microfluidic systems,” *Biophysical Journal* **119**, 493–501 (2020).
- Kumar, M., Walkama, D. M., Guasto, J. S., and Ardekani, A. M., “Flow-induced buckling dynamics of sperm flagella,” *Phys. Rev. E* **100**, 063107 (2019).
- Lagnado, R. R. and Leal, L. G., “Visualization of three-dimensional flow in a four-roll mill,” *Experiments in Fluids* **9**, 25–32 (1990).
- Lee, E. C. and Muller, S. J., “Flow Light Scattering Studies of Polymer Coil Conformation in Solutions in Extensional Flow,” *Macromolecules* **32**, 3295–3305 (1999).
- Milliken, W. and Leal, L., “Deformation and breakup of viscoelastic drops in planar extensional flows,” *Journal of Non-Newtonian Fluid Mechanics* **40**, 355–379 (1991).
- Narayan, S., Moravec, D. B., Dallas, A. J., and Dutcher, C. S., “Droplet shape relaxation in a four-channel microfluidic hydrodynamic trap,” *Phys. Rev. Fluids* **5**, 113603 (2020).
- Pontrelli, G., Ubertini, S., and Succi, S., “The unstructured lattice Boltzmann method for non-Newtonian flows,” *Journal of Statistical Mechanics: Theory and Experiment* **2009**, P06005 (2009).
- Poole, R. J., Alves, M. A., and Oliveira, P. J., “Purely elastic flow asymmetries,” *Phys. Rev. Lett.* **99**, 164503 (2007).
- Reis, T., “On the Lattice Boltzmann Deviatoric Stress: Analysis, Boundary Conditions, and Optimal Relaxation Times,” *SIAM Journal on Scientific Computing* **42**, B397–B424 (2020).
- Sasmal, C., Hsiao, K.-W., Schroeder, C. M., and Ravi Prakash, J., “Parameter-free prediction of DNA dynamics in planar extensional flow of semidilute solutions,” *Journal of Rheology* **61**, 169–186 (2017).
- Schroeder, C. M., Babcock, H. P., Shaqfeh, E. S. G., and Chu, S., “Observation of polymer conformation hysteresis in extensional flow,” *Science* **301**, 1515–1519 (2003a).
- Schroeder, C. M., Babcock, H. P., Shaqfeh, E. S. G., and Chu, S., “Observation of Polymer Conformation Hysteresis in Extensional Flow,” *Science* **301**, 1515–1519 (2003b).
- Tao, S., He, Q., Chen, B., Yang, X., and Huang, S., “One-point second-order curved boundary condition for lattice Boltzmann simulation of suspended particles,” *Computers & Mathematics with Applications* **76**, 1593–1607 (2018).
- Taylor, G. I., “The formation of emulsions in definable fields of flow,” *Proceedings of the Royal Society of London. Series A, Containing Papers of a Mathematical and Physical Character*, 146:501–523 (1934).
- Tretheway, D. C. and Leal, L., “Deformation and relaxation of Newtonian drops in planar extensional flows of a Boger fluid,” *Journal of Non-Newtonian Fluid Mechanics* **99**, 81–108 (2001).
- Tu, M. Q., Nguyen, H. V., Foley, E., Jacobs, M. I., and Schroeder, C. M., “3D manipulation and dynamics of soft materials in 3D flows,” *Journal of Rheology* **67**, 877– (2023).
- Vona, M. and Lauga, E., “Stabilizing viscous extensional flows using reinforcement learning,” *Physical Review E* **104**, 055108 (2021).
- Wang, J., Han, J., and Yu, D., “Numerical studies of geometry effects of a two-dimensional microfluidic four-roll mill on droplet elongation and rotation,” *Engineering analysis with boundary elements* **36**, 1453–1464 (2012).
- Xie, K. and Leonetti, M., “Mechanical characterization of core-shell microcapsules,” *Comptes Rendus. Mécanique* **351**, 163–182 (2023).
- Yu, Y., Qin, Z., Chen, S., Shu, S., and Yuan, H.-Z., “Two-relaxation-time regularized lattice boltzmann model for navier-stokes equations,” *arXiv preprint arXiv:2312.10318* (2023).
- Yu, Y., Qin, Z., Yuan, H., and Shu, S., “Two-relaxation-time regularized lattice boltzmann model for convection-diffusion equation with spatially dependent coefficients,” *Applied Mathematics and Computation* **488**, 129135 (2025).
- Zhao, W. and Yong, W.-A., “Single-node second-order boundary schemes for the lattice Boltzmann method,” *Journal of Computational Physics* **329**, 1–15 (2017).
- Zhou, Y. and Schroeder, C. M., “Single polymer dynamics under large amplitude oscillatory extension,” *Phys. Rev. Fluids* **1**, 053301 (2016).